An investigation of Molecular Magnets Synthesized from Ni(cod)(_2) and the Organic Acceptors TCNQ and TCNQF(_4)

Quinn, Kimberley Jo-Anne

An Investigation of Molecular Magnets Synthesized from $Ni(cod)_2$ and the Organic Acceptors TCNQ and $TCNQF_4$.

Kimberley Jo-Anne Quinn

A thesis submitted in partial fulfilment
of the requirements for the degree of
Master of Science

Department of Physics
Durham University
2009

Declaration

I confirm that no part of the material offered has previously been submitted by myself for a degree in this or any other University. Where material has been generated through joint work, the work of others has been indicated.

Kimberley J Quinn
Durham, August 2009

Acknowledgements

Many thanks to Ian Terry for the opportunity to carry out this project and his continued help and support throughout my time at Durham University. Thanks to Marek Szablewski for synthesis of the materials and helpful discussions.

Thanks to Lian Hutchings, Chris Ottley, Jarka Dostal and Gary Oswald for the TGA, ICP-MS, elemental analysis and XRD measurements.

Thanks also to John Dobson and Charlotte Borgers for their help and support in the lab.

Abstract

Recently a new molecular magnet, Ni_2TCNQ, was reported to be ferromagnetic at room temperatures, with a Curie temperature of 400K[1]. Ni_2TCNQ is synthesized through a wet chemical route using the starting materials, $Ni(cod)_2$ (bis(1,5-cyclooctactadiene)nickel) and TCNQ (7,7,8,8-tetracyanoquinodimethane). This work focuses on the synthesis of this molecular magnet and subsequent characterisation of the magnetic properties.

Several organic acceptor molecules were also examined with the intention of synthesising a new molecular magnet. The chosen organic was $TCNQF_4$, (2,3,5,6-tetrafluoro-7,7,8,8-tetracyanoquinodimethane) due to its small size and magnetic properties. The resulting magnet, Ni_2TCNQF_4, was synthesized following the same procedures as for Ni_2TCNQ with the substitution of TCNQ for $TCNQF_4$.

The magnetic properties for the nickel samples are qualitatively similar and both show ferromagnetic behaviour at room temperature. More specifically the materials exhibit two magnetic phases, in high magnetic fields the materials are paramagnetic and in low magnetic fields exhibit nanoparticulate behaviour. At low temperatures in the paramagnetic phase the materials have been compared to a Brillouin function. This revealed weak ferromagnetic interactions between the spins in Ni_2TCNQ and weak antiferromagnetic interactions in Ni_2TCNQF_4.

In the nanoparticulate phase the materials are superparamagnetic above the blocking temperature, T_b, and below exhibit single domain behaviour. The Curie temperature for Ni_2TCNQ was found to be much higher than previously reported[1], at approximately (625±5) K. The Curie temperature for Ni_2TCNQF_4 was (620±5) K. This suggests that the ferromagnetic phase observed in these materials arises from the nickel nanoparticles present in the material. This conclusion is also supported by XRD and microscopy measurements.

Contents

1. Introduction

Molecular magnets have been designed and studied in the hope of creating materials that exhibit magnetic order at room temperature. Molecular magnets may offer the opportunity to tune magnetic properties through synthesis and offer an alternative to magnets fabricated through high temperature metallurgical routes.

Molecular magnets, sometimes referred to as metal-organic magnets, usually contain an organic acceptor molecule together with an inorganic component such as a transition metal ion. These magnets can generally be classified according to the orbital in which the spins reside[2]. Heisenberg's theory of ferromagnetism[3] explains the necessity for unpaired electrons to reside in the d and f orbitals, as in conventional magnets. However, it is now known that it is possible for a material with electrons residing in only the s and p orbitals to exhibit magnetic ordering[4]. The organic moiety may be an active part in the magnetism with its spins contributing both to the magnetic signal and to the mechanism of spin coupling. Alternatively the organic component may not be directly involved with the magnetic mechanism but only providing the positioning of the metal ions and hence the spins, leading to their magnetic coupling.

The first molecular magnet was $[Fe^{III}(C_5Me_5)_2]^{\bullet+}[TCNE]^{\bullet-}$ (where TCNE= tetracyanoethylene), this magnet has a Curie temperature of 4.8K and exhibits large coercive fields (0.1T at 2K)[5]. This magnet was the first that contained spins in the p-orbital, exhibited magnetic hysteresis, was soluble in organic solvents and did not require metallurgical procassing[6]. More recently a metal organic magnet, Ni_2TCNQ (TCNQ=7,7,8,8-tetracyanoquinodimethane) has been developed, which is claimed to exhibit hysteretic effects at room temperature with an ordering temperature of 480K[1]. One of the goals of the work reported in this thesis is to investigate this claim of room temperature magnetic order.

Molecular magnets may have applications in magnetic storage devices as increased data density requires materials with larger coercive fields[7,8] as demonstrated by molecular magnets such as $[Fe^{III}(C_5Me_5)_2]^{\bullet+}[TCNE]^{\bullet-}$. As organic magnetic materials are insulating there may be applications in transducers to reduce the amount of energy lost through heating. The biocompatibility of some molecular magnets also allows possibilities within medical imaging/implants[7].

2. Literature Review

2.1 Magnetism

There are many different types of magnetism, the various types arise from the variety of ways the electrons in molecules can be coupled together. When placed in an external magnetic field the magnetic dipoles can become partially orientated, this leads to a magnetization, M which is the magnetic dipole per unit volume. The susceptibility, χ, can be used to define the different classes of magnetism such as paramagnetism, diamagnetism and ferromagnetism etc.

Diamagnetism

Diamagnetism occurs in all materials due to the orbital motion of the electrons within an atom. Lenz's law states "when the flux through an electrical circuit is changed, an induced current is set up in such a direction as to oppose the flux change"[9]. The field induced by the current therefore opposes the applied field (as does the associated magnetic moment) and this is diamagnetism. Although diamagnetism occurs in all materials other magnetic effects often overshadow it. The susceptibility of a diamagnetic material is usually small, negative and temperature independent.

Paramagnetism

In the absence of a magnetic field the magnetic moments of the various atoms in a substance are uncorrelated and the net magnetization is zero. In most cases paramagnetism is found in materials whose atoms display unpaired electron(s) and the spins can be considered independent as they are either weakly coupled or not coupled at all[9]. From quantum mechanics it is found that it is not possible for spins to occupy all orientations, only discrete values are permitted. This leads to the magnetic moment of an ion in free space given by Equation 1.

$$\mu = \gamma \hbar J = -g\mu_B J \qquad (1)$$

Where μ is the magnetic moment, γ is the gyromagnetic ratio, $\hbar$ is equal to $h/2\pi$ (1.05459×10^{-34}J s) and J is the total angular momentum of the electron. Also, μ_B is the Bohr magneton and g is the Lande g-factor equivalent to 2.0023 for a free electron. From Boltzmann statistics the average magnetization, M, for a paramagnet can be calculated and is shown in Equation 2.

$$M = NJg\mu_B B_J(y) \tag{2}$$

$$B_J(y) = \left\{\left(1+\frac{1}{2J}\right)\coth\left[\left(1+\frac{1}{2J}\right)y\right] - \frac{1}{2J}\coth\left(\frac{y}{2J}\right)\right\} \qquad y = \frac{g\mu_B J\mu_0 H}{k_B T}$$

$B_J(y)$ is the Brillouin function, μ_0 is the permeability of free space (1.256637×10^{-6}), H is the applied field, k_B is Boltzmann constant (1.38062×10^{-23}JK^{-1}), N is the number of ions per unit volume and T is the temperature, all other constants remain the same as those given in Equation 1. If $y=\mu B/ k_B T<<1$ then this leads to the result shown in Equation 3, where it can be seen that the susceptibility varies inversely with temperature; this is the Curie law.

$$\frac{M}{H} = \frac{NJ(J+1)g^2\mu_B^2\mu_0}{3k_B T} = \frac{N\rho_{eff}{}^2\mu_B^2\mu_0}{3k_B T} = \frac{C}{T} \tag{3}$$

Here C is the Curie constant and ρ_{eff} is the effective number of Bohr magnetons defined as $\rho_{eff} = g[J(J+1)]^{1/2}$. However Equation 3 is only valid for small magnetic fields. At low temperatures and high fields the magnetization is modelled by the full Brillouin function.

In the special case where J=1/2 the Brillouin function reduces from Equation 2 to Equation 4.

$$B_{J=1/2}(y) = \tanh(y) \tag{4}$$

The susceptibility of a paramagnet is small and positive.

In order to discuss further magnetic states relevant to this project it is necessary to introduce the concept of exchange interactions.

Exchange Interactions

Direct Exchange

When two single free atoms are brought together, lobes of charge density that correspond to different electron states overlap. In this region the Pauli exclusion principle must be applied, hence no single electron state may be occupied twice. When the orbital wavefunction is symmetrical the spin wavefunction must be anti-symmetrical (and vice versa) this allows the Pauli exclusion principle to be valid.

Heisenberg introduced the spin Hamiltonian, H, to express the dependence of the spin, S, on the energy splitting[10].

$$H = -2J \sum_{i,j} S_i \cdot S_j. \tag{5}$$

The spin Hamiltonian is electrostatic in origin. Changing the spin symmetry by altering a spin direction must change the orbital symmetry and therefore will redistribute charge. The changes in the Coulomb electrostatic energy of interacting ions act as though there is a direct coupling between the directions of the spins involved.

If J is positive then this leads to ferromagnetic order whereas if J is negative the ordering may be antiferromagnetic or ferrimagnetic. The spin Hamiltonian theoretically justifies the preferred alignment that is made energetically favourable in mean field theory.

Calculations of direct exchange are often too small and of the wrong sign. Therefore it is unlikely to operate in its simplest form in more than a few materials[9].

Indirect Exchange (RKKY Interaction)

The RKKY interaction (named for Ruderman, Kittel, Kasuya and Yosida)[11] occurs in metals through the polarisation of conduction electrons. A local moment, μ, polarises the conduction electrons, if the spins are parallel the wavefunctions of the electrons

will be in-phase. The wavefunctions become out of phase as the distance from μ is increased and will ultimately interfere destructively. This results in an oscillatory behaviour whose magnitude decreases with distance from μ. The distribution of charge density remains constant throughout and the periodicity of the spin density oscillation is determined by the wavelengths of the conduction electrons at the Fermi level.

This mechanism of magnetic coupling has a very long range compared to wavefunction overlap in the direct exchange interaction. If small changes in inter-atomic distance occur it may change both the magnitude and sign of the interaction.

Superexchange

In a system where the ions are too far apart to interact through direct exchange and magnetic ions are separated by a non magnetic ion(s) then the spins may be coupled indirectly by a mechanism known as superexchange. The spins are coupled through intermediate anions.

MnO is an example of a system where superexchange operates. In this case the O^{2-} anion contains outer electrons in a p-state. The charge density of the anion extends outwards either along the bond with the Mn cations (σ-transfer) or perpendicular to it (π-transfer). Each lobe represents one electron per anion and to satisfy the Pauli exclusion principle the two electrons must have opposite spins. The 2p electrons and 3d electrons from the Mn^{2+} cations overlap and mix with electrons of the same spin. When the Mn^{2+} cations have spins antiparallel the total energy is lowered hence leading to antiferromagnetism via superexchange.

Ferromagnetism

In a ferromagnetic material, below the Curie temperature, the spins are parallel to each other in the absence of an external field (Figure 2.1).

Figure 2.1: Alignment of spins in a ferromagnet below the Curie temperature.

Above the Curie temperature, T_c, the susceptibility of a ferromagnet follows the Curie-Weiss law (Equation 6).

$$\chi_V = \frac{C_V}{(T-\theta)} \tag{6}$$

Where χ_V is the volume susceptibility, C_v is the volume Curie constant and θ is the Weiss constant.

As shown in Figure 2.1 in a ferromagnetic material the spins are parallel, however the overall magnetization may be much lower than the saturation magnetization and the application of a magnetic field may be required to saturate the sample. This is due to the formation of small regions within the material known as domains. Due to the different contributions to the energy from anisotropy, magnetic and exchange energy in a ferromagnetic material, it has been shown that the domain formation is a natural consequence[12]. Within each domain the spins are parallel, but the direction of magnetization between each domain may be non parallel. Therefore on a large scale there is no discernible alignment as the domains are orientated randomly. Domain structures lower the overall energy of the system, i.e. from a system with a saturated magnetic moment and a high magnetic energy to a system with a domain configuration with a lower energy[12].

Within a ferromagnetic crystal there are certain directions which the direction of magnetization favours; this is due to anisotropy energy within the material. It is the magnetocrystalline anisotropy energy that directs the magnetization along certain crystallographic axes, known as easy directions. Axes along which it is difficult to produce saturation magnetization are known as hard directions. Magnetocrystalline anisotropy arises as a result from the combined effect of spin orbit coupling and the electric fields associated with neighbouring charged ions. Other types of anisotropy include shape anisotropy and stress anisotropy.

Antiferromagnetism

Below the ordering temperature (or Néel temperature) in an antiferromagnet the spins are aligned antiparallel and the net moment is zero (Figure 2.2), whilst above the Néel temperature the spins are disordered paramagnetically. The susceptibility

follows the law shown in Equation 6 but with a negative θ constant. In a simple antiferromagnet the crystal is divided into two sublattices with one sublattice having spins in a certain direction and the spins in the other sublattice pointing in the opposite direction, therefore nearest neighbour atoms are always antiparallel.

Figure 2.2: Alignment of spins in an antiferromagnet below the Néel temperature.

The susceptibility curve displays a cusp when the temperature is equal to the Néel temperature. Below the Néel temperature the susceptibility is dependent on the field direction relative to the spin axis. If the field is perpendicular to the spin axis then the magnetization is increased in the field direction and the susceptibility remains constant for temperatures equal to the Néel temperature and below. If the field is parallel to the spin axis then the susceptibility increases smoothly to the Néel temperature. If a sufficiently large field is applied the antiparallel moments would be reversed and the system would be comparable to a state with a nearly saturated magnetic moment. In a polycrystalline material the orientation will lie between the limits of a field parallel or perpendicular to the spin axis.

Exchange Bias

When an antiferromagnetic material comes into close contact with a ferromagnetic material some interesting effects can occur. A phenomenon named exchange bias can be observed in layered ferromagnetic/antiferromagnetic systems and core/shell nanoparticles[12]. In nanoparticulate systems the core of the particle may be ferromagnetic with the surrounding shell of the particle antiferromagnetic. Exchange bias causes a shift of the hysteresis loops towards a positive or negative field direction due to exchange coupling of the spins at the interface. When a field is applied the spins that are aligned anti-parallel are weakly affected by the field but the ferromagnetic component will attempt to align with the field. As the ferromagnetic component is exchange coupled to the antiferromagnetic surface the spins must overcome this additional energy before aligning with the field. This causes the hysteresis loop to shift along the field axis. The dependence on particle size, shell thickness among other effects still requires a theoretical explaination[12].

Crystal Field and Spin Transitions

The crystal field effect can be much greater than spin-orbit coupling and leads to the quenching of the orbital angular momentum and the removal of the degeneracy of the *d* orbitals. A transition metal ion with four to seven electrons in its *d* orbital may be in a high spin or a low spin state. The transition between the states is dependent on the energy gap between the metal's orbitals for example e_g and t_{2g}. If the energy gap is larger than the mean spin pairing energy then the electrons occupy the t_{2g} orbitals as these have the lowest energy. In this case Hunds rules are not obeyed and the t_{2g} orbital will be filled first (Figure 2.3). If there are more than six electrons then the higher energy orbital (e_g) will be filled.

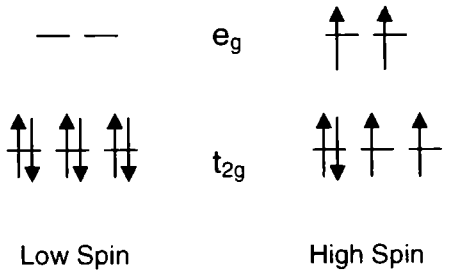

Figure 2.3: Low spin and high spin states in the e_g and t_{2g} orbitals.
(Adapted from Kahn (1993)[15])

In the high spin state the mean spin pairing energy is larger than the energy gap between the e_g and t_{2g} orbitals. Thus it is energetically favourable for the electrons to obey Hunds rules and occupy the orbitals as shown in Figure 2.3.

A spin transition may be induced either by pressure or by temperature and there are various types of transition; the transition may be sudden and occur within a few Kelvin. Alternatively, the transition may occur smoothly across a large temperature range. The transition from one spin state to another may not be complete at either high or low temperatures, although incompleteness at low temperature is more commonly observed[15]. The fraction of the low spin to high spin states as a function of temperature may not be identical depending on whether the material is being heated or cooled and may exhibit a hysteretic effect[15].

Single Domain Particles

Single domain particles are formed when it is no longer energetically favourable for a domain boundary to be formed, a typical size is 10-100nm for digital properites[12]. An ideal single domain particle has a magnetic moment which is directed to one end or the other of the particle. The two permitted directions arise from either uniaxial crystal symmetry or, if the particle is elongated, the direction can arise from (magnetostatic) shape anisotropy. This uniaxial magnetic moment is useful in digital recording media where the different orientations can be labelled as 0 or 1. Single domain particles can exhibit superparamagnetism if the magnetic moment of a unit is constant[12].

If the particles are present in a liquid and free to rotate as a whole then the net magnetization will follow a Langevin function. If the particles are frozen in a solid there will be a remanent magnetization after the applied field is removed.

Stoner-Wohlfarth Model

The magnetization curves of single domain particles with uniaxial anisotropy can be described by the Stoner-Wohlfarth model[16]. The magnetic moment of a particle in a magnetic field will experience a torque, the magnitude of which will be dependent on the angle between the magnetization and the field direction. The strength of the field required to saturate the magnetization in a polycrystalline sample is the field that will force the magnetic moments that lie 90° to the easy axis to align with the field. This field strength (H_s) is given by Equation 7, where K is the anisotropy constant and M_s the saturation magnetization.

$$H_s = \frac{2K}{\mu_0 M_s} \tag{7}$$

If the field is perpendicular to the anisotropy direction then the changes in the magnetization when a field is applied are completely reversible. When the field is anti-parallel to the anisotropy there is an irreversible switching of the magnetization when H_s is larger than $2K/\mu_0 M_s$. In the final situation i.e. when the moment lies at angle to the field that is neither perpendicular nor anti-parallel then the magnetization curve is part reversible and part irreversible. The coercive fields responsible for the

switching of the particles are dependent on the direction of the field compared to the angle of the moment to its easy axis. Stoner and Wohlfarth considered a variety of particles with different directions, each with uniaxial anisotropy and from this the composite hysteresis loop shown in Figure 2.4 was obtained.

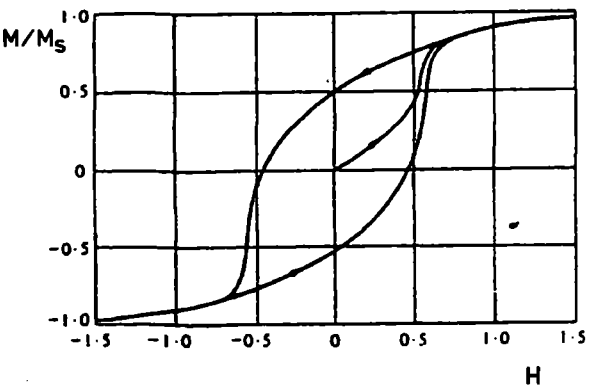

Figure 2.4 Composite hysteresis loop.
(Jiles (1998) pp. 374)[10]

The disadvantage of this theory is the assumption that all the particles are non interacting.

Superparamagnetism

Below a critical particle size a single domain particle's magnetization vector may become unstable and move due to thermal activation. This is due to the thermal energy being sufficient to overcome the energy barrier separating the easy directions of magnetization. This causes spontaneous fluctuations of the magnetization direction. This phenomenon is known as superparamagnetic relaxation and is important in developing high density recording media[17]. The Néel-Brown expression (Equation 8) describes the relaxation of the particles.

$$\tau = \tau_o \exp(E_a / k_B T) \tag{8}$$

Where τ is the time constant, E_a the energy barrier and $\tau_0 \approx 10^{-9}$s. The Néel-Brown expression is valid for particles that are well separated and interparticle interactions are negligible. There are several techniques that can be used to investigate the relaxation properties, however the time scale of the experiment is very important. If

the time scale of the experiment is longer than the relaxation time the magnetization recorded will be the average magnetization for the particles. If the time scale is shorter than the superparamagnetic relaxation then the magnetization may appear static as the particles will not have time to relax during the experiment.

A blocking temperature, T_b, can be defined as the temperature at which the relaxation time is equal to the time scale of the experiment. In other words, for the experimental time scale employed the blocking temperature is that above which the system exhibits superparamagnetism. Above T_b the particles are free to align with the field and behave similarly to a paramagnetic system but with a larger magnetic moment[18].

$$KV \approx 25k_B T_b \tag{9}$$

Equation 9 relates the blocking temperature to the particles volume, V and anisotropy, K. The particle's total anisotropy energy is proportional to its volume. The anisotropy of the particles may vary not only due to the volume but also the particle shape, stress and surface state[17]. This leads to a large variation in the energy barrier distribution and hence a broad distribution of relaxation times.

Experimentally the blocking temperature is revealed as a cusp in the zero field cooled data curve. A zero field cooled (ZFC) data curve is obtained by measuring the magnetization of the sample as a function of temperature. The sample is cooled in the absence of a field, an external field is then applied and the magnetization measured as the temperature is increased. This cusp will be broad if there is a range of energy barriers in the material. The position of the peak is also dependent on the speed at which the measurement is taken. If the measurement is fast then the moments will be unable to relax within the time course of the experiment and therefore the peak will shift to higher temperatures. If the measurement time is reduced then the peak will shift to lower temperatures as the spins will have time to relax.

The Brillouin function may be used to describe the magnetization, however as the available orientations of the magnetism are very close together they appear continuous. This leads to $J \rightarrow \infty$ and the limit of the Brillouin function. The

magnetization can therefore be described by Equation 10 which is known as the Langévin equation.

$$M = N\mu L(y) \tag{10}$$

$$L(y) = \coth(y) - \frac{1}{y} \qquad y = \frac{Jg\mu_B\mu_0 H}{k_B T}$$

Therefore if the magnetization is plotted as a function of H/T magnetization curves recorded at different temperatures should overlay, this analysis can be used to indicate superparamagnetic behaviour.

Spin Glasses

A spin glass is a system with a random distribution of magnetic moments that exhibit frustration. The disorder in the system can either be due to site or bond randomness. Site randomness relates to the distribution of distances between the magnetic spins. Bond randomness is the nearest-neighbour interaction which varies due to either the parallel or anti-parallel coupling[19].

In a metal the RKKY interaction is exhibited by numerous spins within the material, combined with site disorder there is now a random distribution of coupling strengths and directions that lead to frustration. However in an insulating or semiconducting material there are no conduction electrons to allow for the RKKY interaction therefore the mechanism is superexchange.

The magnetic anisotropy present in a spin glass affects the frozen state properties. The dipolar interaction gives a preferential coupling of the moments as a function of angle and will affect magnetic ordering at low temperatures. Yet the dipolar energy is usually weak in comparison to other exchange energies and is considered a secondary effect.

Magnetocrystalline anisotropy imposes certain preferential directions on the magnetic moments due to the crystalline electric field. It is also possible to have a random anisotropy in a non-crystalline material. This is due to the local anisotropy constant

having a distribution of directions and magnitudes that differ at every site giving a range of easy axis that vary depend on the local environment.

As with superparamagnets, spin glasses have a cusp in the zero field cooled data relating to a freezing temperature T_f. Below this temperature the material behaves as a spin glass.

2.2 Molecular magnets

The first model for the possibility of achieving ferromagnetic interactions between organic free radicals was proposed by McConnell[20] in 1963. This model is dependent on radicals with large positive and negative atomic π-spin densities. If the atoms are aligned so that atoms with opposite spin densities can be exchange coupled there should be a resulting ferromagnetic exchange interaction. This model therefore relies on the ability to manipulate the crystal lattice to allow atoms with opposing spin densities to align, producing the ferromagnetic interaction. This model is known as the negative spin density product model. Although it predicts ferromagnetic exchange it does not refer to bulk ferromagnetism which requires ferromagnetic exchange in three dimensions[7]. A second model was developed by McConnell that involves mixing of the ground state with a charge transfer state.

Attempts to create a magnet whose electron spins reside on the p orbital began with TCNQ [4]. The material $[Fe^{III}(C_5Me_5)_2][TCNQ]$ was created and characterised as a metamagnet (a metamagnet having a antiferromagnetic ground state with a transition to a high moment ferromagnetic like state above a critical field value[21]). The observed ferromagnetic state led to theories into how the ground state may be stabilized. One solution involved substituting TCNQ for a smaller radical anion acceptor, TCNE, as this would lead to enhanced spin coupling. TCNE contains the same amount of spin as TCNQ but has a greater spin density as the spins are delocalized over fewer atoms. The resulting material was the first molecular magnet $[Fe^{III}(C_5Me_5)_2]^{\bullet+}[TCNE]^{\bullet-}$ which, as mentioned in the introduction, has a Curie temperature of 4.8K and exhibits large coercive fields (0.1T at 2K)[5].

Following this work there were numerous attempts to create molecular magnets with higher critical temperatures. Some studies substituted Fe^{III} with other metal ions[22,23] and others substituted $[TCNE]^{\bullet-}$ with various radical anion acceptors. Although other

molecular magnets are discussed, the focus of this work will be the use of the transition metal nickel in molecular magnets and the organic acceptor molecule TCNQ.

There have been several studies into $Ni_x[TCNQ]_y$ compounds and numerous papers have been published[2,23,24,25] implementing a wide variety of synthesis techniques. The materials Ni(TCNQ) and $Ni_3(TCNQ)_2$ were synthesized using an electroplating technique[2]. This technique was employed in an attempt to minimise impurities and exert better control over product stoichiometry. However this method results in insoluble complexes that display antiferromagnetic interactions at low temperatures.

Another study into a $Ni_x[TCNQ]_y$ compound characterized $Ni(TCNQ)_2$ which was synthesized using a solution based route[24]. This work reported dominant ferromagnetic interactions at low temperatures with coercive fields of 2.7mT at 2K,[24] the ordering temperature is reported as 24K. The authors claim that competing interactions between the two types of spin centre (nickel and TCNQ), lead to frustration and hence glassiness in the system. This material was therefore characterized by Clerac *et al.* as a spin glass.

Recently a Canadian group have used an unconventional ratio of 2:1 nickel:TCNQ to create the new molecular magnet $Ni_2(TCNQ)$[1]. The authors claim that $Ni_2(TCNQ)$ exhibits hysteresis at room temperature with an ordering temperature of 480K[1] (this value was estimated from magnetic data recorded up to 360K). $Ni_2(TCNQ)$ also exhibits hysteretic effects with coercive fields of 1.4mT and remanent values of $5.49 Am^2kg^{-1}$ at 300K. This molecular magnet was synthesized through a wet chemical route. The basic method involves dissolving TCNQ and $Ni(cod)_2$ in dichloromethane (CH_2Cl_2) and then exposing the solution to air, this leads to the precipitation of small black particles which are collected and dried. The reaction equation can be seen in Equation 11.

$$TCNQ + Ni(cod)_2 \xrightarrow[2.H_2O/O_2]{1.CH_2Cl_2} Ni_2TCNQ.(O)_x.(H_2O)_y.(OH)_z \qquad (11)$$

The material was characterised using a variety of techniques including powder x-ray diffraction measurements which showed the material to be amorphous and the possibility of nickel nanoparticles was also ruled out from spectroscopic studies. The

report suggests that the organic acceptor molecule TCNQ is coordinated to the nickel ions and from the magnetic data, that the organic moiety is not present solely to achieve charge compensation but is inherent to the magnetic structure of the material. From the data the possibility of the magnetization arising from two magnetic regimes could not be discarded but as similar trends in the saturation magnetization have been displayed by other disordered spin glass molecular magnets[25] the authors have classed this molecular magnet as a spin glass.

The group responsible for $Ni_2(TCNQ)$ also investigated the reaction of $Ni(cod)_2$ with the organic acceptor molecule TCNE,[1] see Appendix A1. $Ni_2(TCNE)$ revealed similar properties to those exhibited by $Ni_2(TCNQ)$ with slightly smaller values for the coercivity and remanence at 300K (1.24T and $3.69 Am^2kg^{-1}$ respectively). The authors conclude that this material is also spin glass. A recent paper has since challenged this result[26] claiming that the magnetic properties exhibited by $Ni_2(TCNE)$ do not arise from the organics present in the material. The authors in this study contradict the presence of reduced TCNE in the material as $[TCNE]^{\bullet -}$ is known to react quickly in the presence of water and oxygen to form other products $[C_2(CN)_3O]^-$ that do not enable magnetic ordering[27]. The authors claim that the magnetic properties arise solely due to the presence of nano or greater-sized particles of nickel metal present from the starting materials.

Due to the difficulties in identifying the active magnetic component present in organic and molecular-based magnets it is perhaps not surprising that there are some reports that have been retracted[28] or challenged[26,29]. It is the aim of this research to reproduce and further characterise the Ni_2TCNQ magnet synthesized by Jain *et al.* In addition to this several organic acceptor molecules will be examined in detail to determine their suitability for the synthesis of a new molecular magnet. A new molecular magnet will then be synthesized using nickel and the chosen organic, this new material will then be fully characterised.

When compared to conventional magnets the magnetization of molecular magnets can be directly compared on a per mole basis. However the large molecular weight of molecular magnets means that when comparing saturation magnetization in terms of unit volume or per unit mass the saturation magnetization is much lower. This is due to the lower spin concentration which results in lower magnetizations. The large distances between spins lead to smaller exchange energies and hence low transition temperatures. The organics may also age with time due to their chemical instability. Metal organic magnets may therefore not compare well with existing magnets[7].

2.3 Organic Acceptor Molecules

A variety of organic acceptor molecules will be investigated in preparation for the design and synthesis of a new molecular magnet.

TCNQ (7,7,8,8-tetracyanoquinodimethane) is an organic acceptor molecule. The chemistry of TCNQ has been widely studied due to its interesting conducting properties[2]. The molecule is planar and can be seen in Figure 2.5. TCNQ is readily used in molecular magnets due to the ease at which this compound accepts one electron to form stable crystalline anion-radical derivatives[30]. TCNQ and its fluoro analogue, $TCNQF_4$, have been functionalised with a range of other metals to produce complex stable anion-radical salts.

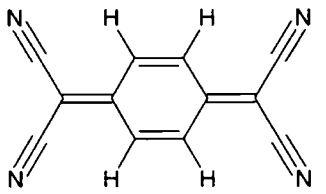

Figure 2.5: TCNQ acceptor molecule

$TCNQF_4$ (2,3,5,6-tetrafluoro-7,7,8,8-tetracyanoquinodimethane) was synthesized by substituting fluorine in place of hydrogen atoms onto the quinoid ring (Figure 2.6a). Fluorine atoms are strongly electronegative therefore it is hoped this molecule will be electron rich.

NaTCNQ (sodium7,7,8,8-tetracyanoquinodimethanide), Figure 2.6b, is a TCNQ molecule with one sodium atom per TCNQ. The sodium atom gives up an electron to the TCNQ molecule in this charge transfer salt.

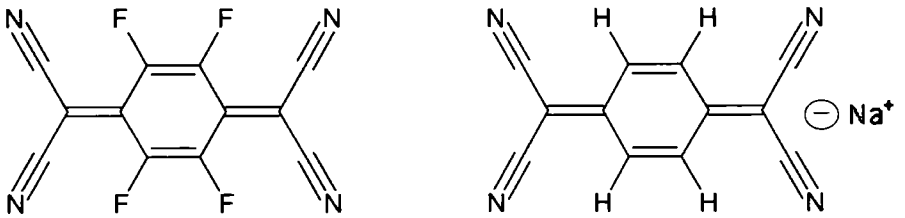

Figure 2.6: a) $TCNQF_4$ b) NaTCNQ

TFDCNQI, ((2,3,5,6-tetrafluorocyclohexa-2,5-diene-1,4-diylidene)dicyanamide) which can be seen in Figure 2.7a, is a small planar molecule with four fluorine atoms. This electron acceptor molecule should be strongly electronegative due to the presence of fluorine.

TCAQ (11,11,12,12-tetracyano-9,10-anthraquinodimethane) was prepared in an attempt to improve the conducting properties of TCNQ derivatives (Figure 2.7b). The π system was extended as it was hoped that this would reduce the intramolecular electron repulsion and hence lead to more stable radicals[31]. However investigations revealed that extending the π system did not improve the acceptor properties and TCAQ displays a more negative reduction potential compared to TCNQ. The non-planar structure of TCAQ has been cited as the reason for the high electrical resistivity and the material behaving as an insulator[31].

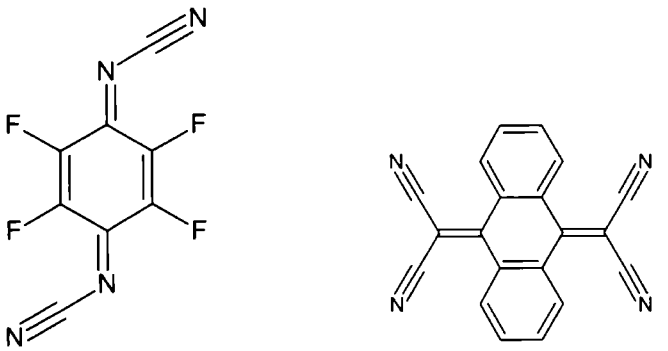

a) b)

Figure 2.7: a) TFDCNQI b) TCAQ

Demi, shown in Figure 2.8, is a diamagnetic electron acceptor molecule. The organic 803(1-(4-Cyano-benzyl)-4-[2-cyano-2-(4-dicyanomethanide-phenyl)-vinyl]-pyridinium) is shown in Figure 2.8b. 803 is a large complex molecule. The final molecule is labelled MSzJ25 and is shown in Figure 2.9. MSzJ25 is the largest molecule investigated.

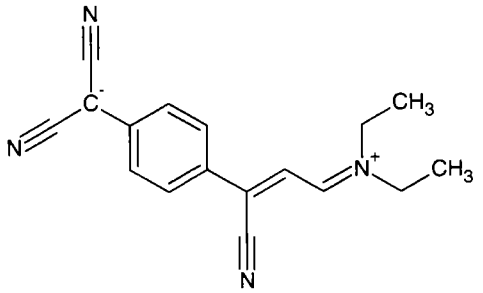

a)

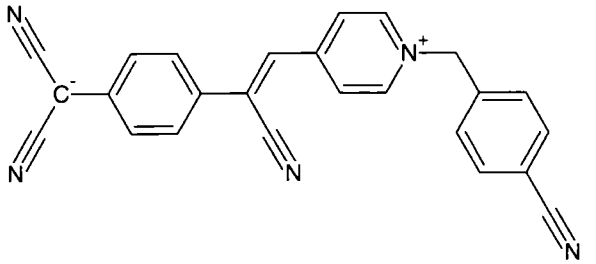

b)

Figure 2.8: a) DEMI b) 803

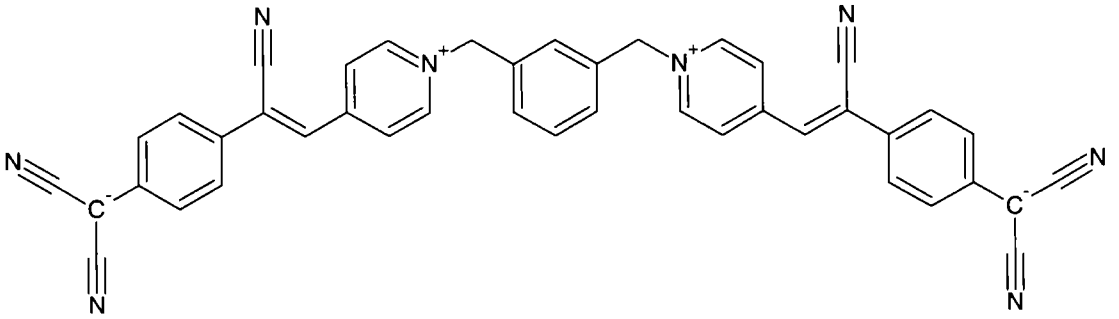

Figure 2.9: MSzJ25

2.4. Experimental Theory

2.4.1 SQUID Magnetometer

The magnetic response of the samples was measured using an MPMS Quantum Design SQUID (Superconducting Quantum Interference Device) magnetometer (see section 3.2). SQUID magnetometers are extremely sensitive and can be used to measure very small magnetic fields.

The SQUID contained in the magnetometer used for this work was an rf SQUID. The SQUID system contains a superconducting ring whose current maintains a constant phase difference. The ring is interrupted by a small layer of insulating film known as a Josephson Junction that allows flux to enter the ring. Two important properties of superconductors are used in the SQUID system; these are magnetic flux quantisation

and Josephson tunnelling. The magnetic flux inside the SQUID loop has discrete values with one flux quanta being equal to 2.07 x 10^{-15} Wb.

The SQUID system is coupled to the inductor of a resonant LC circuit, the output of this circuit depends of the input from the pickup coil. The pickup coil responds to a change in the phase of the current across the Josephson Junction that is caused by a variation in external magnetic flux. Therefore any change in magnetic flux applied to the pick up coil can give a proportional change in the voltage output.

As the SQUID ring is physically small the relative changes in magnetic field are detected using sensing coils that are inductively coupled by a small coil to the SQUID ring. These sensing coils are superconducting and are gradiometrically wound. There are three coils, a large central coil wound in one direction and two smaller coils wound in the opposite direction; this design is employed as to effectively cancel out any uniform external fields.

When a measurement is recorded using the system the sample must be moved through the gradient coils over a distance of approximately 40mm. Therefore the sample length must be less or equal to 5mm in order to prevent inducing a response in the coils that compensate for external magnetic fields. The resultant response from the sample is shown in Figure 2.10. The absolute value of the magnetic moment is then found by fitting the data with the spatial response of a perfect magnetic moment.

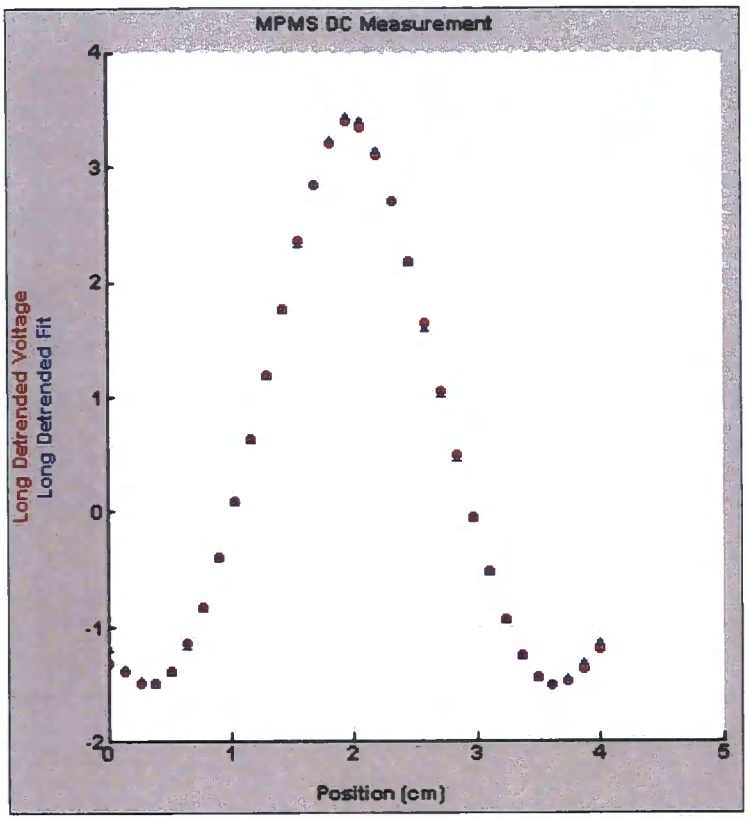

Figure 2.10: Magnetometer fitting to the data, the sample is positioned at 2cm where there is a peak response.

2.4.2 Electron Spin Resonance

Electron spin resonance techniques are able to provide information on materials containing one or more unpaired electrons. The technique is based on the interactions between spins and an applied magnetic field and the interactions between the spins themselves.

For S = ½ and in the presence of an applied magnetic field, the degeneracy is removed and the spins may lie in one of two Zeeman levels. The lowest energy state is given when the spin is anti-parallel to the field (therefore producing a moment parallel to the field) and the highest state is when the spins lie parallel to the field. More electrons occupy the lower energy states due to the Boltzmann distribution which gives the probability of the particle occupying a given energy state. The separation of the Zeeman levels increases linearly with the applied field (Figure 2.11).

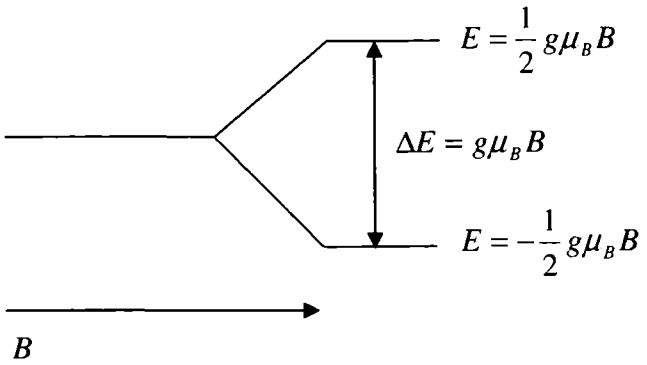

Figure 2.11: Zeeman splitting in an applied magnetic field.

The energy of the state is given by Equation 12, where m_s=±1/2 and g is the free electron g-factor.

$$E = g\mu_B B_0 m_s \tag{12}$$

From the Bohr frequency condition it can be shown that the frequency required for the resonance condition is given by Equation 13.

$$\upsilon = \frac{g\mu_B B}{h} \tag{13}$$

When a sample is exposed to electromagnetic radiation with the frequency required for resonance there will be a sharp peak in the absorption spectra.

In an ESR experiment the sample is exposed to electromagnetic radiation of a fixed frequency and the magnetic field is scanned. When the magnetic field causes the energy difference between the two levels to be equal to that of the incident radiation a transition from one level to another is induced.

The g-factor can be found from a re-arrangement of Equation 13 and is similar in ions which have the same electronic configuration and that are in environments with similar symmetry. The g-factor is only independent of field direction in isotropic materials. For example the g-factor in a single crystal may vary due to anisotropic effects. In this case the crystal would produce a different g-factor for each crystallographic direction. If the sample was in a powder or liquid form then the g-factor is effectively averaged out over all directions. An asymmetric ESR line may suggest that the molecules involved have anisotropic magnetic properties[32].

If the only interaction in the material was an electron with the applied magnetic field then the ESR spectrum would only consist of one line. Other interactions are responsible for the complex spectra attainable, these interactions include the hyperfine interaction. If there were any nuclei in the vicinity of the electron then they would contribute to a local magnetic field. The effective magnetic field experienced by the electron is a summation of the applied magnetic field and that produced by the surrounding nuclei. This interaction between the nuclei and the electron is known as the nuclear hyperfine interaction and may be either isotropic or anisotropic[32]. In a spectrum this interaction may appear as an additional pair of lines, corresponding to the presence of more than two spin energy levels. The more nuclei interacting with the electrons the more the pairs of lines are produced in the spectrum. The number of pairs of line in the spectrum increase exponentially with increasing numbers of nuclei. When the number of nuclei is large a very broad signal is produced.

3. Experimental Details

3.1 Synthesis

3.1.1 Ni_2TCNQ synthesis

The general method of Ni_2TCNQ synthesis is that described by Jain *et al.* 2007[1]. The TCNQ (0.1263g – Lancaster Batch no. 10034078) was weighed and mixed with 100ml dichloromethane (CH_2Cl_2- Aldrich lot 543903-377) producing a yellow solution. The solution was stirred using a magnetic stirrer under an argon atmosphere. The $Ni(cod)_2$ ($Ni(cod)_2$ = Bis(1,5-cyclooctadiene)nickel(0), purchased from Aldrich), a yellow powder, was handled in a nitrogen glove box (as it is known to decompose in air)[26] where 0.324g was measured. The $Ni(cod)_2$ was sealed in a three necked round bottomed flask with three valves to allow for transfer to the fume cupboard where it was placed under an argon atmosphere. When the TCNQ had visibly dissolved in the dichloromethane (approx 40 minutes) the solution was transferred to a funnel. The funnel was attached to the three necked round bottomed flask containing $Ni(cod)_2$, this is the only part of the process where the nickel is exposed to oxygen. However as the container is full of argon, which as it is heavier than air, will likely cover the $Ni(cod)_2$ completely (this appeared to be the case as there was no colour change of the $Ni(cod)_2$ to black which would indicate oxidation). The valve separating the solution from the nickel compound was opened slightly allowing a small amount of TCNQ/ CH_2Cl_2 solution to mix with the $Ni(cod)_2$. There was an immediate colour change to dark green/black. The nickel solution was stirred continuously as the TCNQ and CH_2Cl_2 solution was gradually added. When all the solution was added the mixture was stirred for 3.5 hours and then exposed to air for 2 hours, stirring continuously, this led to precipitation of black particles.

The solution was filtered, the particles washed with dichloromethane and placed in a vacuum to dry, this sample shall be referred to as the dry Ni_2TCNQ sample. The filtrate was left to stand for a further 24 hours, in which time smaller black particles precipitated out of the solution. The filtrate was then filtered, the particles collected and dried in air. This sample is referred to as the wet sample. For both samples the filter paper had a pore size of 11µm, hence the minimum sized particles are of this size.

The only alteration between the method described by Jain *et al*[1]. and the method followed is the addition of the $TCNQ/CH_2Cl_2$ solution to the powdered $Ni(cod)_2$ instead of the powder to the solution. This alteration was simply due to it being easier to control the addition of a solution to a powder.

3.1.2. Ni_2TCNQF_4 synthesis

The method used to synthesize Ni_2TCNQF_4 is similar to that used for Ni_2TCNQ. The $TCNQF_4$ (purchased from Durham Research and Synthesis Ltd) was weighed (170mg) and mixed with 100ml of dichloromethane producing a green solution. The solution was placed in a fume cupboard and stirred using a magnetic stirrer. It was not possible to dissolve the $TCNQF_4$ in the amount of CH_2Cl_2 present in the solution so an additional 100ml was gradually added to dissolve the $TCNQF_4$. Unfortunately not all of the $TCNQF_4$ was dissolved into the dichloromethane and the mixture was cloudy. The solution was filtered (to give a clear solution) and was then added to 315mg of $Ni(cod)_2$, using the same procedures as described previously (section 3.1.1). Whilst the $Ni(cod)_2$ was transferred to the fume cupboard the yellow powder had turned black, suggesting that the $Ni(cod)_2$ may have been oxidised at the surface. This may have been due to a leak in the glove box or a problem with the argon atmosphere in the fume cupboard. Although it was hoped that the $Ni(cod)_2$ would not be oxidised before being mixed with the $TCNQF_4$ solution the final product should not be affected as only the surface of the powder was potentially oxidised. On addition of the $TCNQF_4$ solution to the $Ni(cod)_2$ the solution turned a dark green/black colour. The mixture was stirred for 3.5 hours and then exposed to air for 2 hours, stirring continuously this led to small dark particles forming in the solution. The solution was then filtered, the sample washed with CH_2Cl_2 and placed in a vacuum to dry.

3.2 SQUID Magnetometer

The magnetometer experiments were carried out using a Quantum Design SQUID MPMS (Magnetic Property Measurement System). The temperature range is 1.9 to 400K and with the installation of an external oven the temperature can be raised to 800K. The maximum achievable field is 5T with a field uniformity of 0.01% over 40mm[33].

The samples were placed into gelatine capsules and then compressed and fixed with GE varnish; approximately 2-15mg of sample is needed per capsule. As the organics are expected to be less magnetic than the nickel samples, larger quantities of sample was placed into the capsule. The capsules were then loaded into plastic straws and again held into place with GE varnish. The straws could then be attached to a rod-like sample holder that was inserted into the magnetometer.

The high temperature experiments required the installation of an oven into the magnetometer. The sample loading method also had to be altered due to the straws melting at high temperatures. The samples were loaded into commercial ESR grade quartz tubes. The quartz tubes were modified to contain glass hooks at the opening to allow the tubes to be attached, using nichrome wire, to the rod-like sample holder. The tubes contained a small section of solid quartz to support the sample. This section of quartz provided a small background magnetic signal which was much smaller than the magnetic responses of the Ni_2TCNQ and Ni_2TCNQF_4 samples. Nevertheless, as the magnetization approaches zero the effects of the background signal become much more apparent and the raw data was routinely examined for a shift in peak position that may be caused by the influence of a background signal. As the sample may degrade at higher temperatures the maximum safe temperatures for each sample was determined by Thermogravimetric analysis (TGA).

The SQUID MPMS system can be used for measuring the magnetization as a function of time, $M(t)$, as a function of field, $M(H)$, or as a function of temperature, $M(T)$. $M(T)$ measurements were made after zero field cooling and field cooling the sample. The field cooled (FC) experiment involves cooling a sample down in the presence of a field and then measuring the magnetization as the sample is heated. The zero field cooled (ZFC) experiment involves cooling the sample down in the absence of a field and then applying a magnetic field and heating the sample. Measuring the magnetization as a function of field ($M(H)$) allows, amongst other things, any hysteretic effects of a sample to be investigated. As the magnetometer measures the absolute magnetic dipole moment of the sample the results will be corrected for mass. Therefore the mass magnetization will be quoted in Am^2kg^{-1}.

3.3 Electron Spin Resonance

A Bruker EMX spectrometer was used to record the ESR spectra of the organic acceptors, the wet/dry Ni_2TCNQ samples and the Ni_2TCNQF_4 sample. The spectra were all obtained at room temperature. Approximately 5mg of each sample was loaded into high purity quartz tubes and sealed. The sample was then loaded into the spectrometer and positioned at the centre of the magnetic field. The field was swept whilst the frequency remained constant at approximately 9.75GHz. The spectrum collected showed the first differential of the absorption spectrum. The scans were also repeated to obtain more accurate spectra.

3.4 Infrared Spectroscopy

For infrared spectroscopy a thin disc of the material had to be prepared. Approximately one part sample to three parts potassium bromide was mixed together and ground to produce a fine powder. The powder was then inserted into a mechanical die and compressed forming a thin disc of material. The disc was then loaded into the infrared spectrometer and a spectrum recorded. Infrared analysis was carried out on both of the Ni_2TCNQ samples and Ni_2TCNQF_4.

3.5 TGA

Thermogravimetric analysis (TGA) is an analytical technique that measures the percentage weight change of a sample as a function of temperature. TGA was completed on the wet and dry Ni_2TCNQ samples and the Ni_2TCNQF_4 sample using a Perkin Elmer Pyris 1 TGA analyser. The typical precision of this machine is approximately ±0.001mg over a temperature range from room temperature to 1073°C with heating rates of up to 80K/min. Approximately 6-18mg of each sample was used for the TGA and the percentage weight change was measured as a function of temperature. The sample was heated at a rate of 10K/min across the temperature range of 298-1270K.

3.6 ICP-MS

Inductively coupled plasma mass spectroscopy (ICP-MS) was performed on a Perkin Elmer Elan 6100 DRC Plus ICP Mass Spectrometer. Both the Ni_2TCNQ and Ni_2TCNQF_4 samples were tested for their percentage nickel content using this technique.

3.7 XRD

X-ray powder diffraction patterns were obtained for the Ni_2TCNQF_4 sample using a Bruker d8 Diffractometer. A thin covering of the sample material across a holder was required for this technique. The sample holder was made from glass, which superimposes an amorphous background onto the results which is removed during data analysis.

3.8 Electron Microscopy Measurements

Scanning electron microscopy (SEM) measurements were recorded on the dry Ni_2TCNQ and Ni_2TCNQF_4 samples. In preparation for the SEM measurements the samples were loaded onto silicon chips and held into place with carbon sticky tape. The chips were then placed in a vacuum for 48hrs to make sure the sample stays in position. The chips were coated with platinum to a thickness of 2nm, allowing electrical conduction and preventing the build up of charge.

For the Transmission Electron Microscope (TEM) measurements the samples were dissolved in dicholormethane followed by sonication for 10 minutes. A grid was then dipped into the solution and allowed to dry, effectively suspending the sample in the grid. It is worth noting that it is possible the larger particles may sink to the bottom of the solution thus preventing them from being loaded onto the carbon grids.

4. Results and Analysis

4.1 Organic Acceptor Molecules

ESR Results

The ESR spectra of the various organic acceptor molecules were recorded at room temperature. Unfortunately it was not possible to obtain a precise g-factor as the ESR did not contain an accurate frequency counter. The g-factor is calculated from Equation 13 and therefore the inaccuracy in the determination of the frequency leads to an unreliable g-factor. Attempts to calibrate the various g-factors with the stable free radical diphenylpicrylhydrazyl (also known as DPPH with a known g-factor of 2.0036) were also unsuccessful. It was found that from run to run the system parameters changed slightly and as the microwave cavity could only support one sample at a time the system would change again with the replacement of DPPH. The g-factors were recorded together with the linewidth of the signal and are displayed in Table 4.1.

Organic Acceptor	g-factor	Linewidth ($x10^{-4}$T)
TCNQ	2.0054	6.4±0.7
$TCNQF_4$	2.0036	11.8±0.9
TFDCNQI	2.0075	53.2±1.3
TCAQ	2.0016	35.1±1.1
DEMI	2.0048	58.5±3.8
803	2.0045	59.4±2.6
NaTCNQ	2.0038	21.1±0.8

Table 4.1: The g-factors and linewidths of the various organic acceptor molecules.

One sharp peak is displayed in the TCNQ spectrum with a small line width consistent with the presence of a free radical. The free radical g-factor is equal to 2.0023. The peak is symmetric and was fitted using the WinSim software[34] to one species as can be seen in Figure 4.1a.

The background signal of the TCNQ sample revealed an increase in the background signal with increasing fields; this could be due to magnetoresistance. Magnetoresistance is when the electrical resistivity of conducting and semi

conducting solids changes when a magnetic field is applied. The change in conductance of the material is dependent on the square of the magnetic field[35].

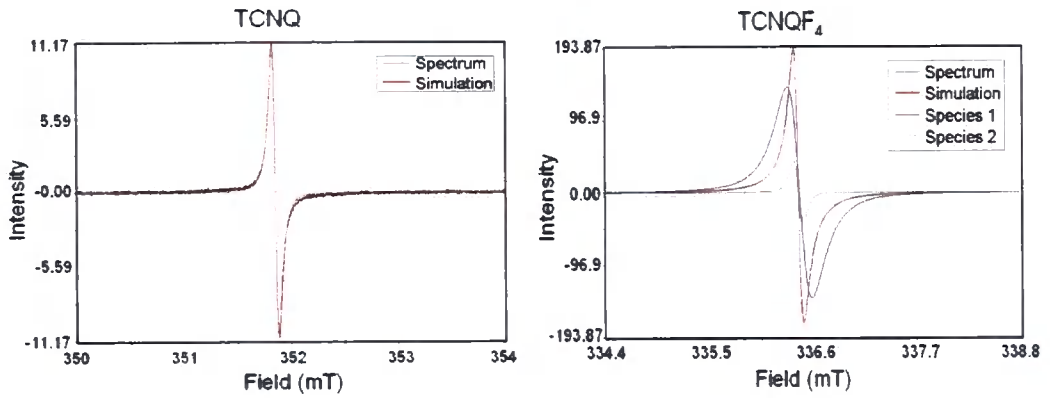

Figure 4.1: Room temperature ESR spectrum of a) TCNQ b) $TCNQF_4$.

The ESR spectra of $TCNQF_4$ can be seen in Figure 4.1b and displays a peak corresponding to more than one free radical in the sample. The WINSIM software was used to fit the data but required two different species to fit the data accurately. The linewidths of the two species are $(8.1\pm1.1)\times10^{-4}$ T and $(12\pm0.8)\times10^{-4}$ T with specie areas of 73.4 and 26.6 respectively. The background signal of the sample was zero and field independent. The ESR spectrum of TFDCNQI was also fit using the WINSIM software and required two species for an accurate fit. The linewidths of the two species are $(31.3\pm2.8)\times10^{-4}$T and $(47.9\pm2.7)\times10^{-4}$T with specie areas of 40.2 and 23.0 respectively.

The organics 803 and DEMI displayed peaks corresponding to free radicals in the samples. Both molecules are large and have similar g-factors. The molecules were fit with one species and displayed similarly large linewidths. The large linewidths arise from the many components present in the materials. The background signal was constant for both samples.

The ESR spectra for TCAQ revealed peaks in the data associated with free radicals. The background of the spectra was complicated and not able to be fitted using WINSIM. TCAQ is a large molecule with many different components that could cause such a complicated spectrum.

NaTCNQ contained a large peak corresponding to the presence of free radicals in the sample. There was also some hyperfine interaction evident in the spectra

indicating interactions between electrons and their environment. Unfortunately due to the complicated spectra the data was not able to be fitted using WINSIM. The background throughout the field range measured was constant.

Magnetic Measurements

The magnetization as a function of field, $M(H)$, and of temperature, $M(T)$, was investigated for each of the organic acceptor molecules. The field applied during the field cooled (FC) and zero field cooled (ZFC) experiments was $\mu_0 H$=1T. Where possible the $M(H)$ curves were examined at temperatures of 4 and 300K and $M(T)$ curves were recorded between 2-300K.

$M(T)$ and $M(H)$ curves showed anomalies in the data as the magnetization approached zero, this was due to the magnetometer struggling to fit the data. It is likely this occurred due to the increasing influence of the background signal as the sample response approaches zero. The background signal becomes dominant and the magnetometer fits to this signal. This can be seen in the raw data as a shift in the apparent position of the sample (from 2 cm as can be seen in Figure 2.10). When the field changes to a finite value it is the sample that provides the dominant signal and the raw data shows the position of the sample to be in the original place. This increase in background signal could, for example, be observed in the TCNQ data as the magnetization approached zero in the field dependence $M(H)$ plots, therefore the data at and approaching M=0 is unreliable and excluded.

The diamagnetic contribution to the magnetism was calculated by plotting susceptibility against inverse temperature. This was done for each of the organics investigated, with the intercept revealing the diamagnetic susceptibility. An example can be seen in Figure 4.2a for NaTCNQ. Each of the data sets was also fit to the Curie Weiss law (Equation 6) by plotting the inverse susceptibility against temperature (after correction for the diamagnetic contribution). Figure 4.2b shows the resulting graph for NaTCNQ.

The values for each of the organics are tabulated for comparison in Table 4.2 and Table 4.3.

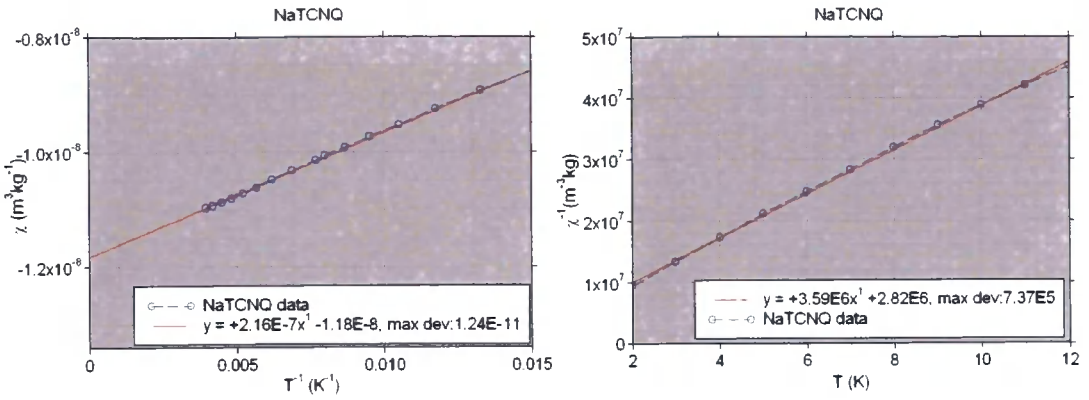

a) b)

Figure 4.2: a) Susceptibility against inverse temperature for NaTCNQ, intercept is the diamagnetic susceptibility. b) Inverse against temperature for NaTCNQ. The data is then fit to Equation 6 to determine the Curie and Weiss constants.

Organic Acceptor	Diamagnetic Susceptibility ($x10^{-8}m^3kg^{-1}$)
TCNQ	-0.772±0.004
$TCNQF_4$	-3.61±0.03
TFDCNQI	-1.03±0.01
TCAQ	-1.42±0.01
DEMI	-9.50±0.01
803	-1.61±0.03
MSzJ25	-8.23±0.07
NaTCNQ	-1.18±0.01

Table 4.2: Diamagnetic susceptibility of the organic acceptor molecules.

Organic Acceptor	Mass Curie Constant ($x10^{-7}$ m^3Kkg^{-1})	Number of magnetic entities per unit mass (kg^{-1})	Number of formula units per unit mass (kg^{-1})	Weiss Constant (K)
TCNQ	0.029±0.002	$(3.64±0.26)x10^{20}$	$2.95x10^{24}$	-0.03±0.01
$TCNQF_4$	2.51±0.11	$(3.21±0.14)x10^{22}$	$2.18x10^{24}$	-4.41±0.04
TFDCNQI	1.32±0.01	$(1.69±0.02)x10^{22}$	$2.64x10^{24}$	-0.92±0.04
TCAQ	1.67±0.02	$(2.13±0.03)x10^{22}$	$1.98x10^{24}$	-0.93±0.05
DEMI	0.22±0.02	$(2.80±0.27)x10^{21}$	$2.18x10^{24}$	-1.86±0.08
803	1.28±0.01	$(1.64±0.02)x10^{22}$	$1.56x10^{24}$	-4.94±0.14
MSzJ25	70.9±9.1	$(9.06±1.17)x10^{23}$	$9.37x10^{23}$	-0.62±0.08
NaTCNQ	2.61±0.04	$(3.33±0.06)x10^{22}$	$2.95x10^{24}$	-0.85±0.14

Table 4.3: The calculated Curie and Weiss constants and N values of the organic acceptor molecules.

The $M(T)$ curves of TCNQ, 803, TFDCNQI and MSzJ25 reveal that the materials are diamagnetic with a paramagnetic component at low temperatures. The field cooled and zero field cooled curves superimpose suggesting that the materials do not exhibit remanent components. Figure 4.3 displays the FC ZFC curves for TCNQ. At 60K there is a slight discrepancy between the curves this may be due to the sample changing position in the magnetometer. This appears in the raw data as a permanent shift in the position of the magnetic moment.

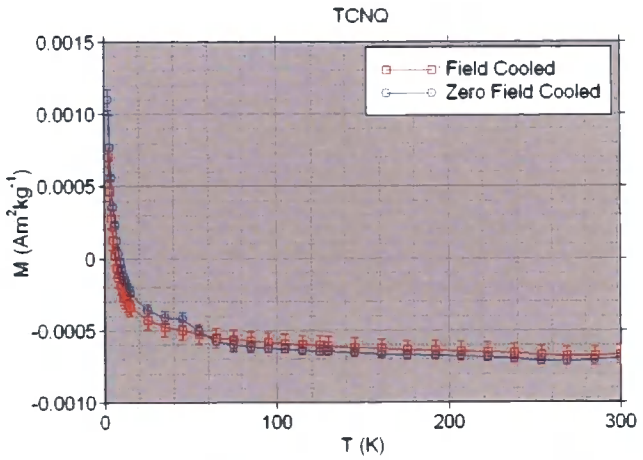

Figure 4.3: $M(T)$ curves for TCNQ at an applied field of $\mu_0 H$=1T.

For all the organics investigated the $M(H)$ curves did not display any hysteretic behaviour, but some displayed anomalies in the data as the magnetization approached zero. This is due to the fitting of the background signal as previously described (page 32, paragraph 2) and the appropriate data points were removed. The low temperature $M(H)$ data for the 803 and MSzJ25 samples was difficult to analyse due to large errors (calculated by the magnetometer). These errors may have resulted from the many components present in these samples.

803 provides the highest value Weiss constant from all the organic acceptor molecules. The value of (-4.94±0.14) suggests that the spins are aligned antiferromagnetically and are interacting strongly with each other. This value implies that at temperatures below 4.94K there would be indication of magnetic order in this material. However from the magnetic data there is no evidence of magnetic order. The large value of the Weiss constant may be due to clustering of the spins in this material. It is possible that areas are present in the sample where the spins are close together and interacting. At temperatures below 5K it may be these spins providing the signal, thus leading to the larger value for the Weiss constant. It is possible that

these clusters of spins are far apart in the material and not interacting over long distances, this would lead to the apparent lack of evidence of magnetic order in these materials. The number of spins per kilogram is also lower than would be expected for a radical per molecule.

The Curie constant in Table 4.3 was used to estimate the number of magnetic entities contributing to the magnetic signal per kilogram, N, from Equation 3. The number of formula units per kilogram was also calculated and is shown in Table 4.3. Many of the organic acceptor molecules have a similar Curie constant and the values for N can be directly comparable to the number of formula units per kilogram. The number of formula units may be higher than the number of magnetic entities as it is possible only one electron is contributing to the signal per two formula units.

MSzJ25 has the largest calculated Curie constant of $(70.9\pm9.1)\times10^{-7}$ m^3Kkg^{-1}. This large value suggests that this organic molecule contains many free radicals in comparison to the other organic systems, this is shown by the high number of magnetic entities contributing to the signal. When comparing the calculated N value $(9.06\pm1.17)\times10^{23}kg^{-1}$ to the estimated number of formula units $(9.37\times10^{23})kg^{-1}$ they are nearly equal, suggesting that there is one electron contributing to the signal per formula unit.

It was observed that TCAQ and DEMI were diamagnetic throughout the temperature range examined. There was a slight separation in the FC ZFC curves for both of these samples that suggest they may contain a remanent component. The $M(H)$ loops confirmed the diamagnetic properties of the samples at temperatures of 4 and 300K.

The FC ZFC curves for $TCNQF_4$ superimpose as can be seen in Figure 4.4. The magnetization is positive throughout the $M(T)$ plot therefore the sample has a large paramagnetic component

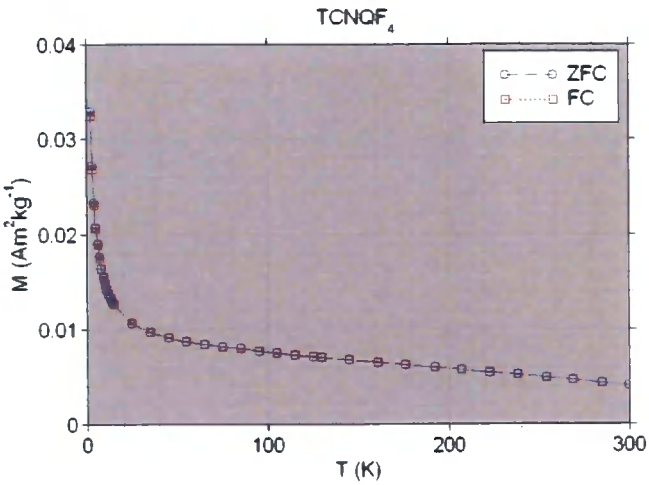

Figure 4.4: $M(T)$ curve for $TCNQF_4$ with an applied field of $\mu_0 H$=1T (Corrected for diamagnetic susceptibility).

Perhaps the most interesting of the organics investigated is NaTCNQ. The ZFC FC curves superimpose and reveal that the material is paramagnetic at low temperatures. The magnetization decays to zero at higher temperatures when corrected for diamagnetic susceptibility.

The theoretical volume Curie constant is given by Equation 3. If the mass Curie constant is divided by the density it is possible to obtain the Curie constant in terms of volume and therefore the number of magnetic entities per unit volume can be estimated (Equation 14). Konno and Saito[36] report a value for the density of 1480 kg m^{-3}.

$$N = \frac{3C_m k_B}{\mu_0 \mu_B^{\ 2} \rho_{eff}^{\ 2} \rho} \tag{14}$$

Where C_m is the mass Curie constant, N is the number of magnetic entities per unit volume, ρ is the density and all other constants remain the same as Equation 3. Inserting the experimentally found Curie constant (Table 4.3) together with the calculated ρ_{eff} value (J=1/2, g=2, therefore $\rho_{eff} = g[J(J+1)]^{1/2}$=1.732), and the value for the density into Equation 14, a value for N is found to be N=(2.25±0.04)x$10^{19}$$m^{-3}$.

As a comparison the number of NaTCNQ units per m^3 was estimated using values provided by Konno and Saito[36], this resulted in an N value of (3.91x10^{27}) m^{-3}. The number of NaTCNQ units per metre^3 is directly comparable to the number of electrons per metre^3 as there is one electron per NaTCNQ unit. The experimental

value for N ((2.25±0.04)x$10^{19}$$m^{-3}$) is much less than the value calculated from Konno and Saito (3.91x10^{27} m^{-3}). This may be due to the quality of NaTCNQ crystals that were used in the experiment. Defects in the crystal can trap conduction electrons and as it is these electrons which are providing the magnetism, N will be decreased.

The $M(H)$ curves exhibit paramagnetic behaviour at low temperatures (Figure 4.5a) in which the magnitude of the magnetization decreases as a function of increasing temperature. At 300K the sample is diamagnetic as shown in the field dependence plots (Figure 4.5b), this indicates that the sample goes through a spin transition. At 300K the curve in the data at low fields may be due to the magnetometer struggling to fit data at such low magnetization values, or alternatively the sample may be contaminated with a small ferromagnetic species.

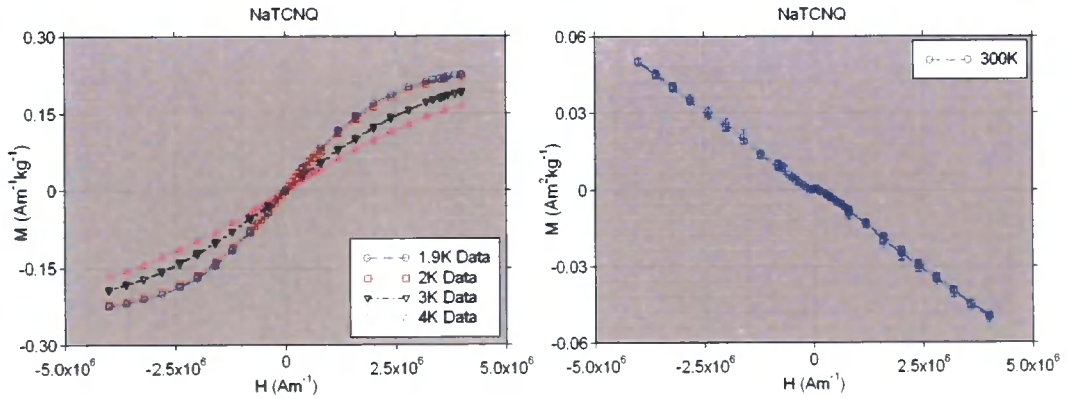

Figure 4.5 $M(H)$ curve for NaTCNQ at a) 1.9-4K and b) 300K.

The low temperature data has been corrected for diamagnetism and compared to a Brillouin function with J=1/2 and θ=-0.85±0.14. To begin comparing the curves an initial value of N was taken to be that found using the Curie Weiss fitting (N=(3.33±0.06)x10^{22} kg^{-1}) but to obtain good agreement between the curves it was necessary to slightly reduce the N value to N=(2.58±0.01)x10^{22} kg^{-1} (Figure 4.6a).

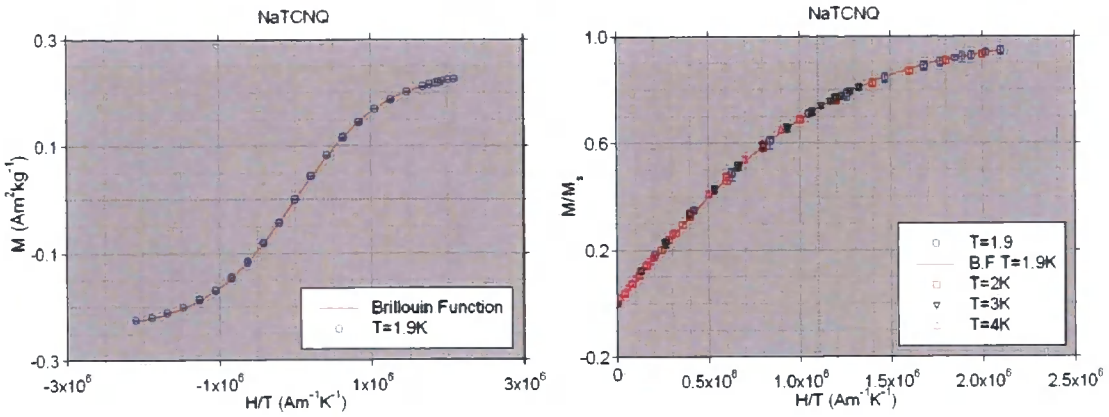

a) b)

Figure 4.6: a) $M(H)$ curve at 1.9K with Brillouin function, J=1/2.
b) M/M_s against H/T for various temperatures, M_s=0.23Am^{2}kg^{-1}.

For a simple paramagnetic system the plot shown in Figure 4.6b should produce a graph in which all the curves at different temperatures overlay. The value for the saturation magnetisation, M_s, was taken to be 0.23 Am^{2}kg^{-1} (from 1.9K data). The plot also contains the Brillouin function at T=1.9K with θ=-0.85±0.14.

4.2 Wet Ni_2TCNQ

Elemental analysis determined the percentage mass of particular elements in the wet Ni_2TCNQ sample, the results of which can be seen in Table 4.4. Jain *et al*[1] formulated an estimate of the empirical composition of the material based upon values obtained through elemental analysis. The resulting composition is reported as $[Ni_2(TCNQ).(O).(OH).2H_2O.(CH_2Cl_2)_{0.125}]$ or $[Ni_2(TCNQ).(OH)3.H_2O.(CH_2Cl_2)_{0.125}]$, there are two compositions as analytically equivalent oxygen species cannot be distinguished, i.e. $[H_2O + O^{2-} + OH^-]$ versus $[3OH^-]$. The calculated values shown in Table 4.4 are those reported in the literature, as calculated using the formulae mentioned above.

Nitrogen can be considered a good marker for the percentage of TCNQ in the sample as it is the only element, available for testing, that is found only in TCNQ. Carbon and hydrogen can also be found in the dichloromethane. The percentage of nitrogen in the sample is slightly low, this could be due to an increase in solvent in the sample. Chlorine atoms are large; therefore if additional solvent was present, the total mass percentage of the other elements would be decreased.

Using the nitrogen value as a marker for the percentage of TCNQ in the material it is possible to calculate the expected values of carbon and hydrogen that would be present due to the presence of TCNQ alone. This revealed a value for the percentage of carbon in the TCNQ of 29.80%. If the percentage carbon due to dichloromethane and that found in TCNQ is subtracted from the total carbon found in the sample a deficit of 4.95% is revealed. The increase in carbon present is likely found from the starting material $Ni(cod)_2$ (where $(cod)_2=(C_{12}H_8)_2$). The same analysis was completed on the hydrogen in the sample but the percentages involved were too small for conclusive results.

Element	Calculated %	Found %
C	36.30	35.12
H	2.32	2.38
N	13.96	11.59
Total %	52.58	49.09

Table 4.4: Elemental analysis for the wet Ni_2TCNQ sample.

The ICPMS data reveals the percentage of nickel in the sample (Table 4.5). The percentage is slightly high compared to the calculated value.

Element	Calculated %	Found %
Ni	27.9	29.6±0.7

Table 4.5: ICPMS data for the wet Ni_2TCNQ sample.

By using the nitrogen percentage found in the elemental analysis the total percentage of TCNQ in the sample was calculated. By comparing this value to that found for the percentage nickel, the ratio of Ni:TCNQ can be determined. This analysis concludes that the ratio of Ni:TCNQ is 2.3:1.

TGA of the sample revealed a significant 9% decrease in mass between 300 and 620K, corresponding to water loss (Figure 4.7a). The second stage of decomposition occurs at approximately 620K. The safe temperature to heat the sample to in the magnetometer was therefore determined to be 580K, thus preventing the sample from the second stage of decomposition.

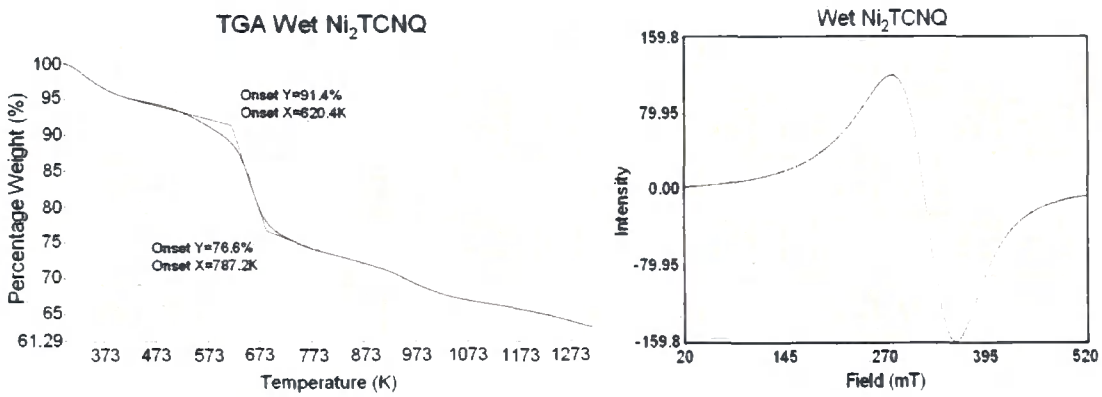

a) b)

Figure 4.7: a) TGA of the wet Ni_2TCNQ sample b) ESR spectrum of wet sample.

The electron spin resonance spectra (Figure 4.7b) revealed a large absorption of the microwave radiation across a wide magnetic field range. Unlike the organic molecules, the ESR signal is not singularly due to an organic free radical which would have a narrow line width centred at approximately 2.0023. The signal is slightly asymmetric with a linewidth of 0.076T. The broad signal may be a result of the interactions between the two types of spin centres.

The infrared spectra of the wet Ni_2TCNQ sample is shown in Figure 4.8a. There is a broad ν_{CN} band at 2169cm^{-1}, this verifies the presence of TCNQ. This band is higher in energy than that of $TCNQ^0$ (2222cm^{-1}) suggesting that the sample contains reduced TCNQ [37]. The spectrum also displays a peak at 1503cm^{-1} corresponding to a $\nu_{C=C}$ stretch which is indicative of $TCNQ^{\bullet-}$. A δ_{C-H} feature can be seen at 825cm^{-1}. Both the $\nu_{C=C}$ feature and the δ_{C-H} stretches are traits of the pi-delocalised TCNQ moiety. The broad peak at 3200cm^{-1} corresponds to the presence of water in the sample.

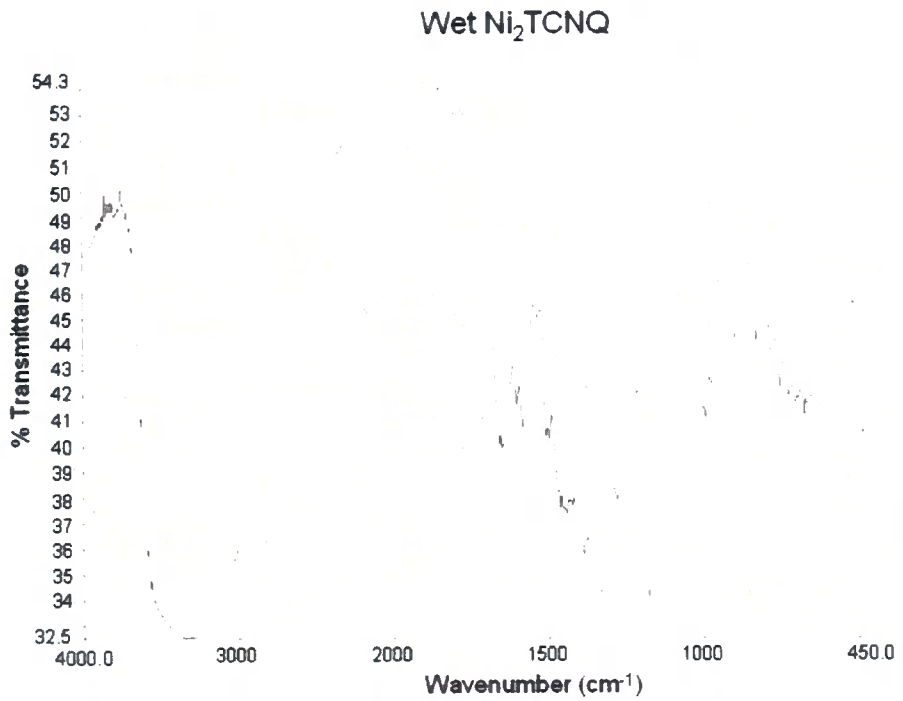

Figure 4.8: Infrared spectrum of the wet Ni_2TCNQ sample.

Magnetic Measurements

The magnetization as a function of temperature ($M(T)$) was investigated for field cooled and zero field cooled experiments at an applied field of $\mu_0 H$=2.5mT (Figure 4.9), following the procedures of Jain *et al.* There is a maximum in the ZFC data at approximately (210±5) K. This is the blocking temperature (T_b), this feature could indicate either a glassy magnet or a superparamagnet as both regimes display a cusp in the ZFC data. Above T_b the curves are aligned and the magnetization decreases until it reaches the Curie temperature. An extrapolated value shows the Curie temperature to be in the region of (417±5) K. There is also an increase in the susceptibility in the field cooled data at low temperatures.

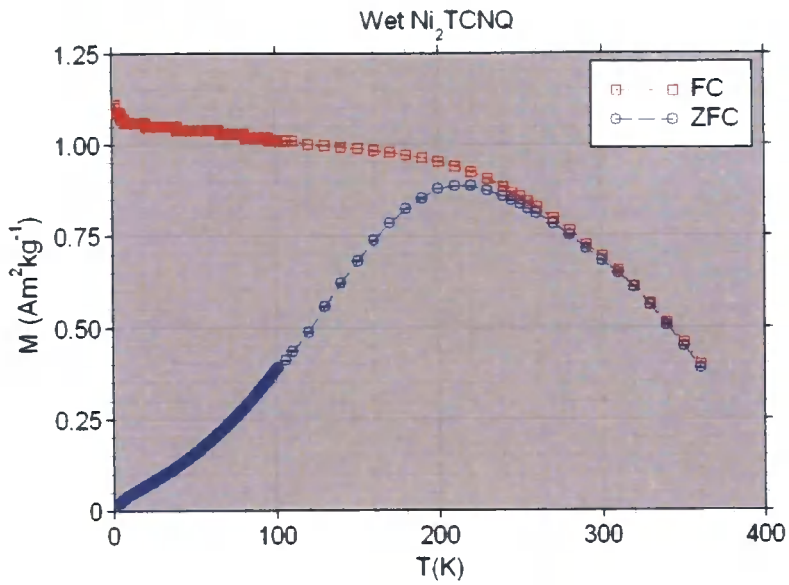

Figure 4.9: $M(T)$ curves for wet Ni_2TCNQ with an applied field of $\mu_0 H$=2.5mT and a heating rate of 1K/min.

Jain *et al.*[1] reported a value of 330K for the blocking temperature. However this value is not directly comparable with the data as the experimental parameters are not defined i.e. the heating rate.

When the heating rate was increased to 10K/min the cusp in the ZFC data shifted to a value of (245±5) K, this is not unexpected. The experiment is dynamic, the spins are associated with a relaxation time, τ. If the timescale of the experiment is fast compared to the spins fluctuating then the blocking temperature will be shifted to higher values, as the spins are unable to relax within the time course of the experiment. When the experiment is slowed down the spins relax within the time restraint and the cusp in the ZFC data is shifted to lower temperatures (see section 2.1 on superparamagnetism). The broad cusp in the ZFC data is mostly likely due a distribution of particle sizes, each associated with a different relaxation time.

The sample was heated to increasingly high temperatures in an attempt to more accurately determine the Curie temperature.

Figure 4.10a displays the FC ZFC curves at 480K. The actual value for the Curie temperature is above the estimated value obtained by extrapolation from lower temperature measurements. It is possible that the magnetic response is due to the Ni_2TCNQ paramagnetic susceptibility dominating at temperatures above the extrapolated Curie temperature; especially as the applied field is 2.5mT, however

differences between zero field cooled and field cooled data could signify that this is not the case. To avoid destroying the sample before determining the Curie temperature, the sample was heated in stages. $M(H)$ loops were recorded before and after each high temperature $M(T)$ experiment to assess the sample. For example in Figure 4.10b the sample was heated to 480K between loops.

The decrease in magnetization in Figure 4.10b is most likely due to the sample decomposing at the higher temperature of 480K. It is also possible that the mass of the ferromagnetic component is decreasing as the sample decomposes; the mass magnetization is still evaluated using the original mass leading to a lower mass magnetization. The sample was heated to 580K but had still not reached its Curie temperature. This contradicts current literature that the Curie temperature is approximately 480K[1].

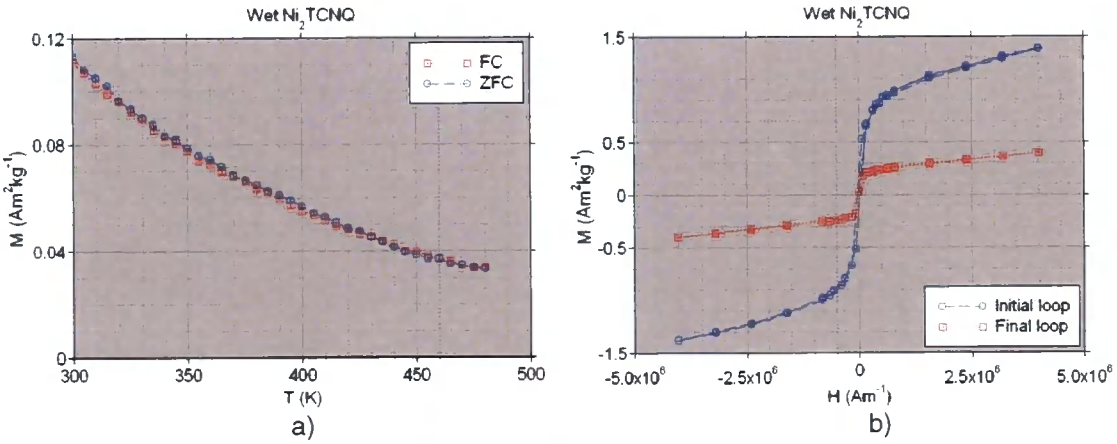

Figure 4.10: a) $M(T)$ curves for wet Ni_2TCNQ, $\mu_0 H$=2.5mT and a heating rate of 1K/min. b) 420K $M(H)$ loops taken before and after a 480K $M(H)$ loop.

$M(H)$ loops were recorded across the whole available temperature range (2-360K-without installation of the oven) and in high applied fields (up to 5T). The $M(H)$ loops are typical of soft magnetic materials and show a strong paramagnetic component present at high fields, Figure 4.11a.

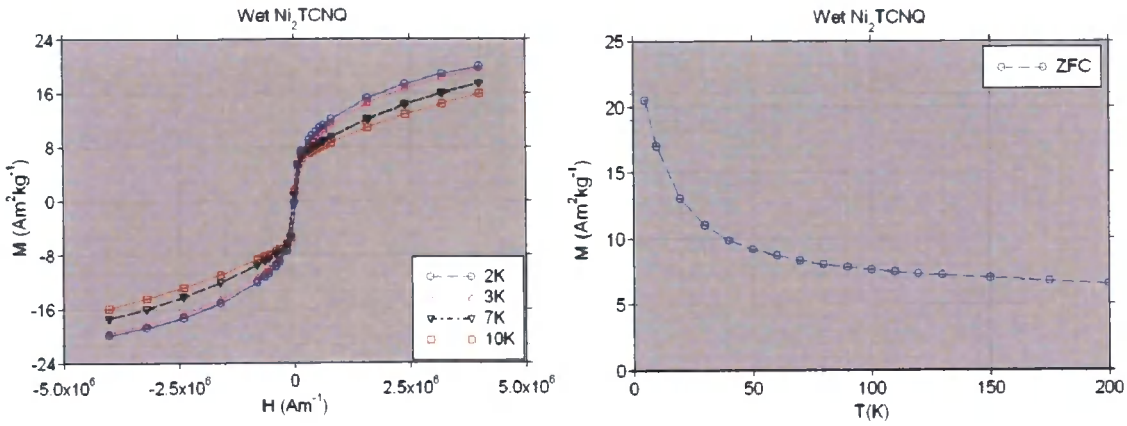

a) b)

Figure 4.11: a) Low temperature $M(H)$ loops: maximum applied field of $\mu_0 H$=5T. b) Zero field cooled $M(T)$ curve with $\mu_0 H$=5T.

The paramagnetic component present at high fields is demonstrated in Figure 4.11b. The ZFC data was repeated at an applied field of 5T, at this field there is a strong paramagnetic component dominating the magnetism. The system also exhibits a remanent component.

The magnetic data examined so far suggests there are two magnetic phases in this material. A paramagnetic component dominating at high fields and at low fields a nanoparticulate component that gives rise to the blocking temperature. The spread of data points about the blocking temperature indicate that the sample contains a variety of different sized particles.

The following data sets were recorded in low applied fields to explore the nanoparticulate contribution to the magnetization. An $M(H)$ loop at 2K displays single domain behaviour (Figure 4.12). The linear area at the start of the loop is consistent with the sample containing multiple particle sizes with spins pointing in many directions. Particles with moments lying perpendicular or at small angles to the field will slowly align with the external field as it is increased; this causes the linear dependency of the loop in the first quadrant. Towards higher field values the larger particles with high coercivities may still not be aligned with the field. Therefore the energy required to rotate the direction of the magnetic moment to align with the field has not been reached. The sample displays coercivities of (30±1) mT at 2K.

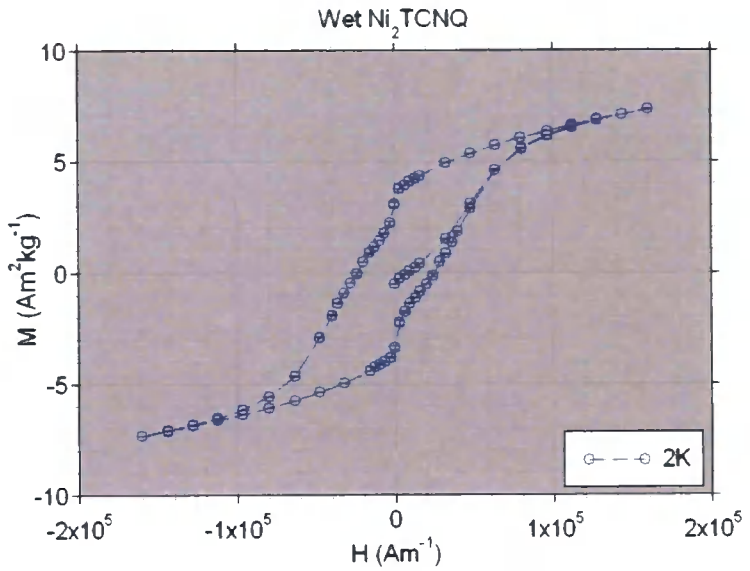

Figure 4.12: 2K $M(H)$ loop at low fields.

It is likely that the discontinuity in the curve as the field approaches zero is due to the small coercivity of some particles. When a negative field is applied the moments with small coercivities change direction immediately. The speed of the experiment determines whether certain moments flip between measurements. If the experiment was slowed down/more points recorded there would be more discontinuity in the curve as when the field approaches zero the particles would have more time to relax. If the experiment was sped up a smooth curve would replace the sudden drop in magnetization.

The $M(H)$ loop in Figure 4.12 is comparative to the composite hysteresis loop which models a distribution of Stoner Wolfgarth particles. This loop is constructed by considering all possible orientations of the particles magnetic moments relative to the easy axis. A feature of the loop is that the remanence is half the value of the saturation magnetization (see Figure 2.5).

The $M(H)$ loop is reproducible at 2K and at other temperatures of 5, 7 and 10K. This reproducibility contradicts the previous possible conclusion that the material is a spin glass, as in that case the $M(H)$ loops would not be expected to be reproducible[19].

When analysing the coercivities of the sample at various temperatures a slight shift in the loop towards positive field values is observed. This shift is between 0.9-2.4mT and may be a result of exchange bias. It is possible the nanoparticles have a shell that is magnetically different from the core resulting in antiferromagnetic interactions

between the two. Alternatively the nanoparticles may be magnetically coupled to the paramagnetic matrix in which it is embedded. This may result in the particle having to overcome additional energies at the surface before aligning with the field, thus resulting in a shift in the $M(H)$ loops.

As shown in Figure 4.11 in high magnetic fields the sample exhibits paramagnetic behaviour, in an attempt to model the paramagnetic contribution the data was compared to a Brillouin function. The function, with J=1, was adapted slightly to that given in Equation 2 to take into account the contribution to the magnetization from the nanoparticulate component (Equation 15).

$$M = NgJ\mu_B\left[\left(\frac{3}{2}\coth\left(\frac{3y}{2}\right)\right)-\frac{1}{2}\coth\left(\frac{y}{2}\right)\right]+M_{s(Nano)} \qquad (15)$$

$$y=\frac{g\mu_B J\mu_0 H}{k_B(T-\theta)}$$

$M_{s(Nano)}$ is the saturation magnetization of the nanoparticulate component and all other constants remain as in Equation 2.

The $M_{s(Nano)}$ value must be included in the function as the paramagnetic component is in addition to the underlying nanoparticulate contribution. The saturation magnetization value for the nanoparticles is taken from data recorded at a low temperature and low applied fields, where there is minimal paramagnetic contribution and was found to be $M_{s(Nano)}$=(6.2±0.1) Am^2kg^{-1}.

Theoretical Brillouin function curves are shown in Figure 4.13, with parameters chosen to achieve the closest concurrence with the data. Good agreement with the experimental data is generally obtained, though there is a slight deviation from the curve at low fields. This is not unexpected as at low fields the paramagnetic contribution no longer dominates. The closest agreement between theory and experimental is found when θ=1.1±0.2K, which suggests weak ferromagnetic interactions between the magnetic moments with J=1. The dependence of the function on the value of θ is demonstrated in Figure 4.13b.

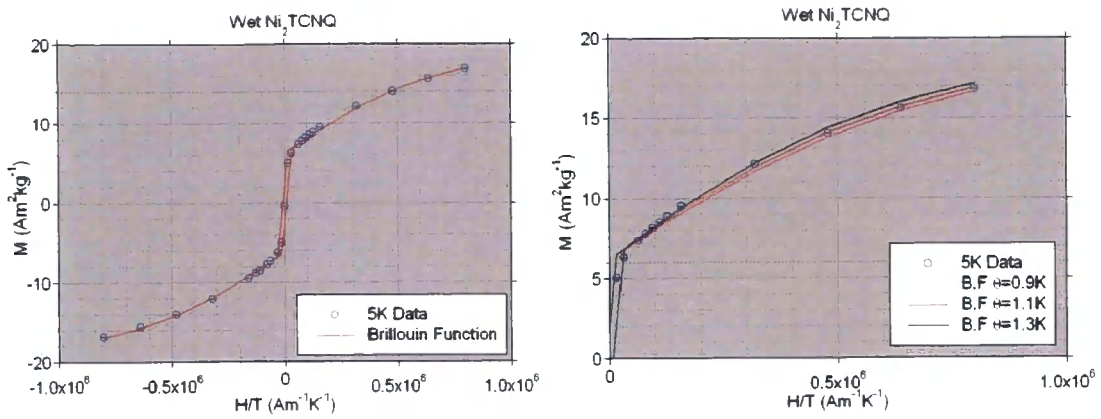

a) b)

Figure 4.13: a) $M(H)$ curves at 5K for wet Ni_2TCNQ, maximum field value of $\mu_0 H$=5T and Brillouin function with J=1, θ=1.1±0.2K. b) Dependence of θ on Brillouin function.

The data are modelled with the assumption that the nickel ions are present in a crystalline electric field and are isolated with a quenched orbital momentum leading to a value of J=1. The Brillouin function achieves closest agreement with the data with an N value of (7.2±0.2)x10^{23} kg^{-1}, suggesting that there are this many magnetic entities contributing to the magnetic signal with a J value of 1. Elemental analysis determined the percentage of nickel in the sample to be (29.61±0.69)%, from this value an estimate of the number of nickel atoms per unit mass was found to be (3.04±0.07)x$10^{24}$$kg^{-1}$.

The N value used in the function was found by comparing the Brillouin function to the data, where it is assumed that J=1 and the N value is essentially a scaling factor in the function. The J value is taken to be one as the nickel is assumed to be in a 2+ state[1], however this may not be the case. If the J value was not actually equal to one then the theta parameter may in reality be compensating for the changing J value.

In the plots shown in Figure 4.14a the curves should all overlay for a simple paramagnetic system, but this is not the case. $M_{s(Para)}$ is the paramagnetic saturation magnetization value of the material taken to be (22±1) Am^2kg^{-1}, from 2K data. The function begins at approximately 0.25 instead of zero due to the underlying nanoparticulate component.

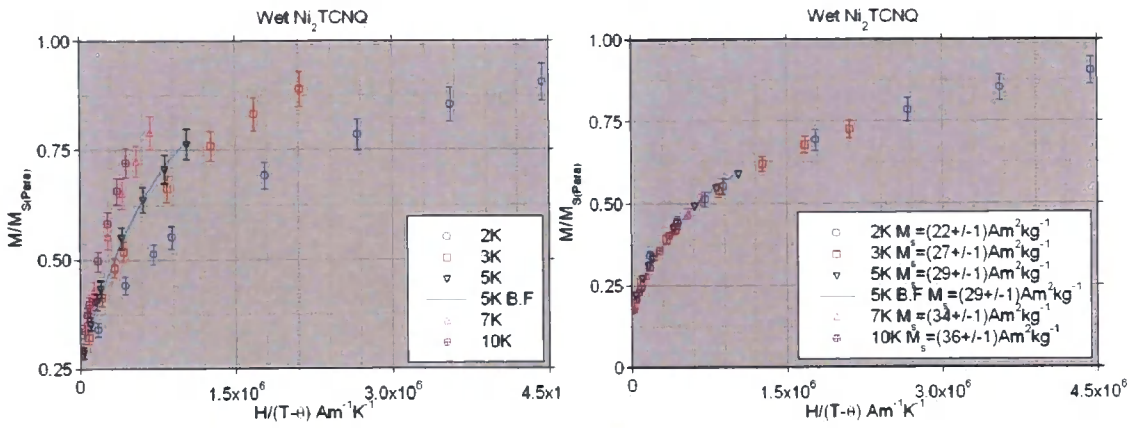

a) b)

Figure 4.14: a) Temperature plots with $M_{s(Para)}$ fixed at (22±1) Am^2kg^{-1} and θ=1.1K (from Brillouin function). b) The same plot whilst varying $M_{s(para)}$ B.F. is the Brillouin function at 5K with J=1.

To overlay the curves the paramagnetic saturation magnetization has to be increased with temperature (Figure 4.14b). $M_{s(para)}$ is dependent on the N and the J values. If the value of J was changing as a function of temperature then this would imply that the shape of the curve is changing (as J is contained within the coth function in the Brillouin function - see Appendix A2). If N were changing then the shape of the function would not be altered, as N is a scaling factor in the equation (Equation 19). It appears from Figure 4.14a that the shapes of the curves are not altered and by scaling through M_s they overlay. Graph 4.14b provides evidence that J=1 and that when comparing the Brillouin function it is the number of magnetic entities per unit mass that is changing, therefore the theta parameter is valid.

The increase in paramagnetic saturation magnetization with increasing temperature is indicative of a thermally induced spin transition from a low spin state (LS) to a high spin state (HS). A possible interpretation is that a J=0 to J=1 transformation is occurring upon increasing T. Such a model could be described by a fixed value of J=1, but with a temperature dependent number of magnetic entities. Spin transitions are seen in other transition metal complexes and can be induced by not only temperature but also light irradiation[38] and pressure[39].

The magnetization of the sample is changing with time, as can be seen in Figure 4.15. The two loops are identical yet in the initial loop it can be seen that the

magnetization has decayed slightly from when the field was first increased in the positive field direction to the completion of the loop thus indicating that something in the sample has altered. The final loop was recorded two weeks after the initial loop and the decay in magnetization is apparent.

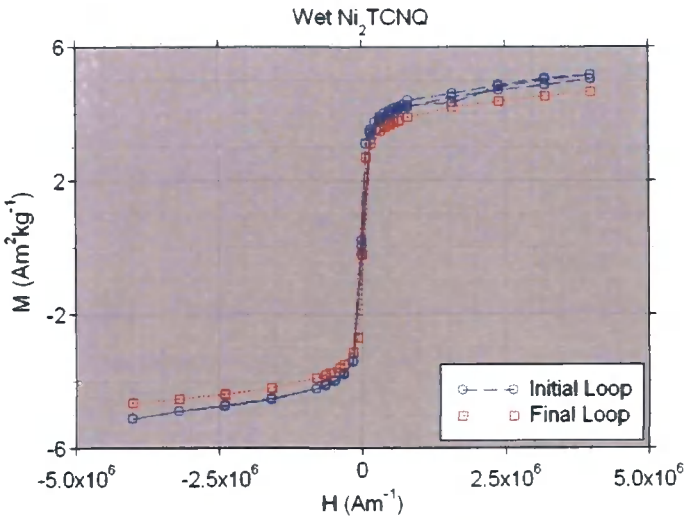

Figure 4.15: $M(H)$ loops for wet Ni_2TCNQ at 360K. The loops were recorded two weeks apart.

After careful consideration it was decided that the sample could be heated to higher temperatures (up to 630K) in a final attempt to discover the Curie temperature. The magnetization as a function of temperature can be seen in Figure 4.16. This experiment revealed the Curie temperature to be (625±5)K for the wet Ni_2TCNQ sample, much higher than the extrapolated value suggests.

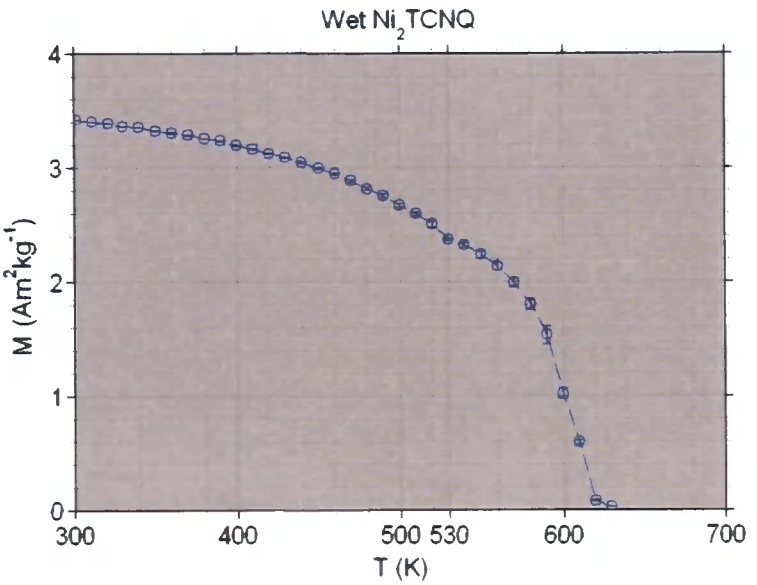

Figure 4.16: $M(T)$ Wet Ni_2TCNQ sample.

The Curie temperature for nickel is approximately 631K[40]. Therefore there is a strong possibility that the nanoparticulate component in this sample is nickel. From Equation 9 an estimate can be made of the particle size. Using the anisotropy for nickel ($5.1 \times 10^3 Jm^{-3}$)[10], and the blocking temperature (210±5) K the estimated particle size is approximately (24.2±0.2) nm.

There is also a dip in the $M(T)$ data around 530K, this is potentially an additional Curie temperature for another component in the sample. If the dip in the data at 530K is indeed another Curie temperature superimposed on the curve then this would suggest that there is another component in the sample that is interacting ferromagnetically. One interpretation is that this is indeed the ferromagnetic phase attributed to the Ni_2TCNQ complex.

4.3 Dry Ni_2TCNQ

The results of the elemental analysis for dry Ni_2TCNQ are given in Table 4.6. It is expected that this sample would contain less solvent material than wet Ni_2TCNQ due to the synthesis method (this sample was dried in a vacuum thus effectively removing any solvent). The higher nitrogen content suggests there is less solvent in the dry sample in comparison to the wet. Using the nitrogen value as a marker, the calculated percentage of carbon in the sample (due to the TCNQ moiety) is 31.37%. Taking into account the percentage carbon due to the dichloromethane this leads to an excess of 4.17% carbon in the sample. As with the wet sample it is assumed that the increase in carbon is from the $Ni(cod)_2$.

Element	Calculated %	Found %
C	36.30	35.91
H	2.32	2.43
N	13.96	12.20
Total %	52.58	50.04

Table 4.6: Elemental analysis for dry Ni_2TCNQ.

The ICP-MS result, shown in Figure 4.7, suggests that there is an increase in nickel in the dry sample. Although this may be the case it is possible that this sample contains less solvent which would account for the increase in percentage nickel.

Element	Calculated %	Found %
Ni	27.93	33.79±0.30

Table 4.7: ICPMS data for the dry Ni_2TCNQ sample.

The ratio of nickel to TCNQ in the sample is calculated from the ICP-MS data and the nitrogen values determined through elemental analysis. This leads to a ratio of 2.8:1 Ni:TCNQ in the dry Ni_2TCNQ sample.

The TGA of dry Ni_2TCNQ (Figure 4.17a) is very similar to the wet sample. Analysis revealed a percentage change corresponding to water loss at approximately 300-520K. The second stage of decomposition began at 600K therefore the safest temperature was determined to be 580K.

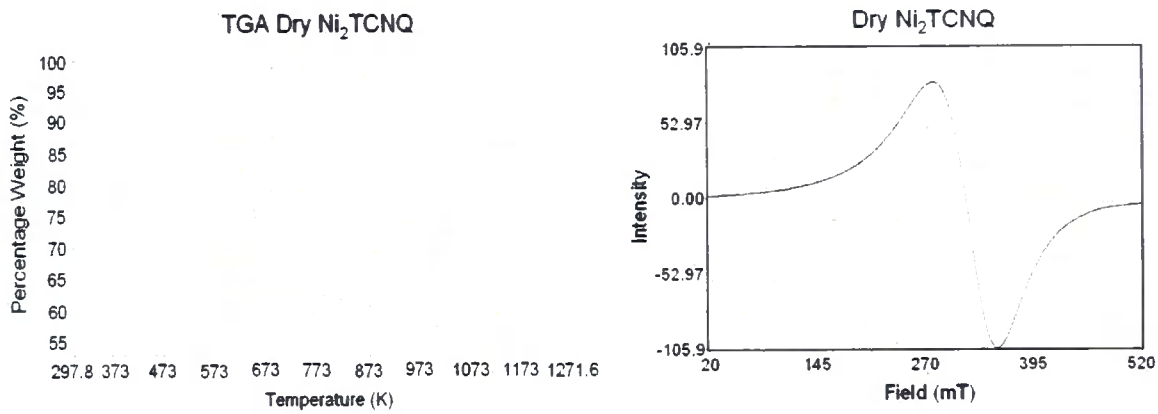

a) b)

Figure 4.17: a) TGA of dry Ni_2TCNQ b) ESR spectrum of dry Ni_2TCNQ.

The room temperature ESR spectrum (Figure 4.17b) was recorded for dry Ni_2TCNQ and is very similar to the wet sample. The signal is broad with a linewidth of 0.073T indicating interactions between the two spin centres. The signal is also asymmetric.

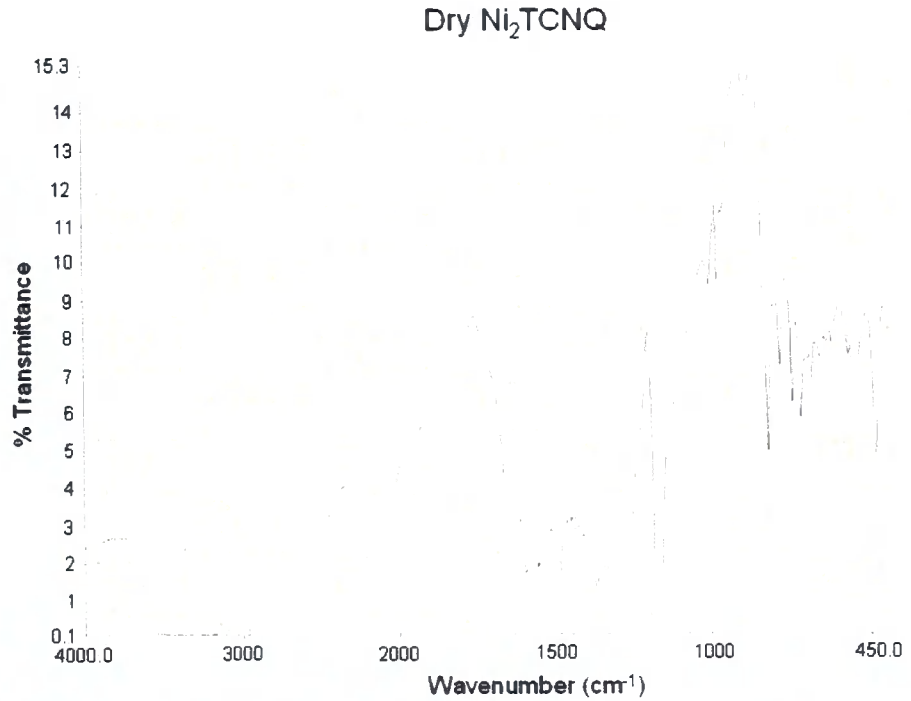

Figure 4.18: Infrared spectrum for the dry Ni_2TCNQ sample.

The infrared spectrum (Figure 4.18) revealed a $\delta_{C\text{-}H}$ feature at 824cm^{-1} and a $\nu_{C=C}$ stretch at 1504cm^{-1}, both of which are characteristic of the pi-delocalised TCNQ moiety[2]. As with the wet Ni_2TCNQ sample the absence of a peak at 2220cm^{-1} and the presence of a peak at 2158cm^{-1} suggests that the TCNQ in the sample has been reduced. The presence of water in the sample is confirmed with a broad peak at approximately 3200cm^{-1}. With this sample it was possible to resolve part of the fingerprint region, which confirmed the presence of C-H.

Magnetic Measurements

$M(T)$ plots were used to estimate the blocking temperature of dry Ni_2TCNQ and are shown in Figure 4.19a. There is a broad maximum about T_b due the range of particle sizes in the sample. The blocking temperature was found to be (230±5) K and thus higher than T_b for the wet sample at the same heating rate. As the blocking temperature is proportional to the particles volume this suggests that dry Ni_2TCNQ contains larger particles than the wet sample. Using Equation 9 the particle size is estimated to be approximately (25.0±0.2) nm. From extrapolation of the curves the Curie temperature is estimated to be approximately (418±5) K.

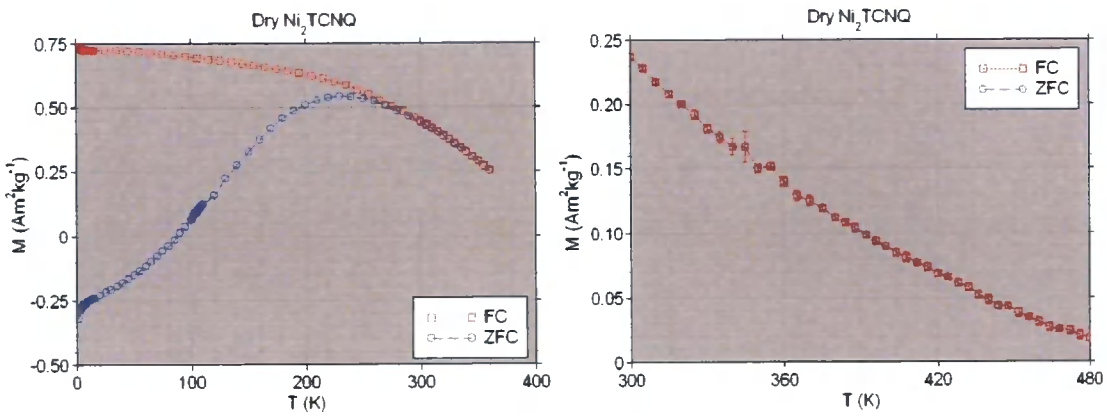

a) b)

Figure 4.19: $M(T)$ curves with an applied field of $\mu_0 H$=2.5mT and a 1K/min heating rate for dry Ni_2TCNQ. a) Low temperatures b) High temperatures.

The dry sample was heated to higher temperatures in an attempt to deduce the Curie temperature. The $M(H)$ loops recorded before and after increasingly high temperatures (<360K) demonstrate a decrease in magnetization after the sample is heated. The Curie temperature is above 480K as can be seen in Figure 4.19b.

The $M(H)$ loops reveal a strong paramagnetic component at high fields (Figure 4.20a). At lower fields and below the blocking temperature, the sample displays single domain particulate behaviour (Figure 4.20b). In this regime the material displays large coercivities ((47±0.1) mT at 2K) and remanence. The system is similar to a distribution of Stoner Wolfarth particles, with the remanence of the system approximately equal to half of the saturation magnetization. There is a range of particle orientations with respect to the easy axis, therefore the loop is comparative to the composite hysteresis loop shown in Figure 2.5.

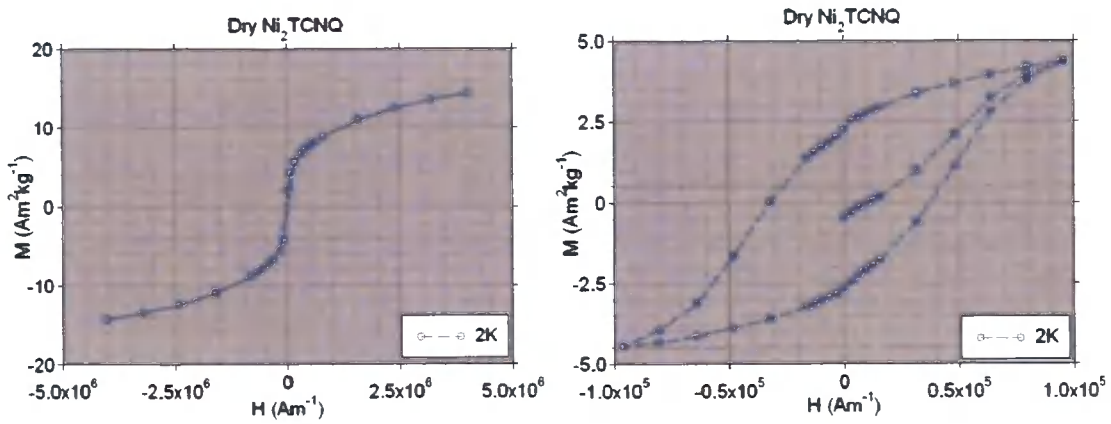

a) b)

Figure 4.20: a) $M(H)$ loops at 2K for dry Ni_2TCNQ a) Applied field value up to $\mu_0 H$=5T. b) Applied field value up to $\mu_0 H$=0.1T

In Figure 4.20b the initial magnetization is formed as the randomly orientated particles slowly align with the field. The loop has not reached saturation due to hard particles with high coercive fields. When compared to the wet sample the $M(H)$ loop of the dry sample has not closed at the highest field value, this again suggests that there are larger particles in the dry Ni_2TCNQ (c.f. fig. 4.12). It proved difficult to accurately calculate the saturation magnetization of the nanoparticulate component in the material as when the field was increased to higher values the paramagnetic component begins to contribute to the magnetic signal. When analysing the coercive field data the coercive fields are slightly larger in the positive field direction ((0.7-7.0) mT) thus causing the loop to shift to the right. This may be a result of exchange bias in the system similar to that observed with the wet sample.

The high field paramagnetic data was compared to a Brillouin function with J=1 (Figure 4.21a). An $M_{s(Nano)}$ value of (4.2±0.1) Am^2kg^{-1} calculated from the low temperature, low field data was used in the function. The best agreement between

the function and the data is achieved with a value of θ=1.9±0.4K and N=(5.6±0.1)x10^{23} kg^{-1}. From elemental analysis the number of nickel atoms per kilogram is estimated to be (3.47±0.03)x10^{24} kg^{-1}. The value for theta is positive suggesting that ferromagnetic interactions exist in the paramagnetic compound as observed with the wet sample. Note that the fit is poor towards lower field values due to the influence of the nanoparticulate contribution. As with the wet Ni_2TCNQ sample the J value is fixed at J=1 and it is assumed that it is the N value together with θ that creates agreement between the experimental data and theory. Further analysis shows this assumption to be accurate as the curves at different temperatures superimpose in Figure 4.21b.

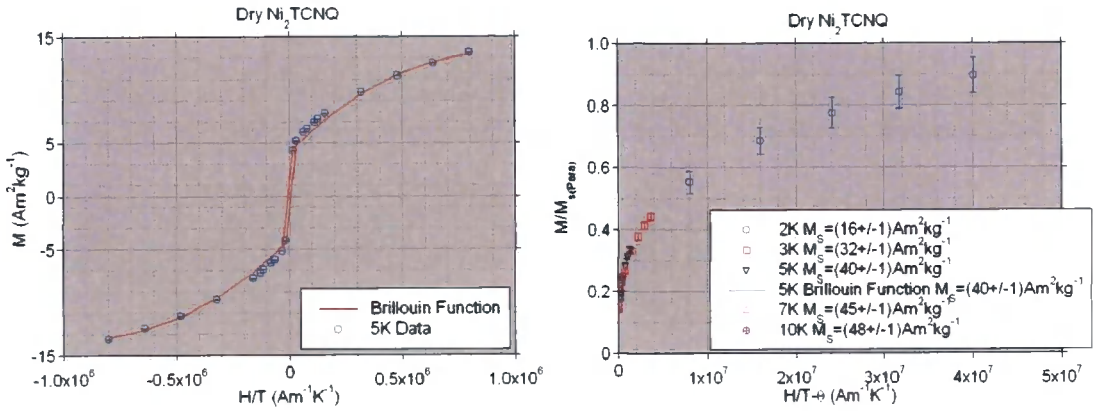

a) b)

Figure 4.21: a) Brillouin function at 5K, J=1 and θ=1.9K. b) Temperature plots with M_s altered to superimpose curves with θ=1.9K.

To superimpose the curves in Figure 4.21b it is necessary to scale $M_{s(Para)}$, thus the saturation magnetization is increasing with temperature. This suggests that the number of magnetic entities contributing to the magnetic response is increasing with temperature. This characteristic is indicative of a low spin state to a high spin state transition, as observed with the wet sample.

Microscopy Images

Scanning electron microscopy images reveal a large distribution of particle sizes as demonstrated in Figure 4.22. From the images an estimate of particle sizes show the range to be between (90±5) nm for smaller particles to (215±5) nm for the larger particles.

Figure 4.22: SEM images of Ni_2TCNQ illustrating the spread of particle size.

Current literature[1] states that the particles have a texture like "broken mud", a similar texture can be seen in Figure 4.23. The cracks in the surface may be due to the sample drying out and the solvent evaporating after synthesis. The sample appears as though it may have a layered structure (see Appendix A3), this could be due to the synthesis method and the sample settling over time.

Figure 4.23 shows the backscattered electron images. The light areas correspond to areas with a high Z number and it is possible that these areas relate to nickel particles. A secondary electron image is generally required as the topology of the material can also cause such bright spots (Figure 4.23b). There are several areas which are densely populated in the backscattered electron image but not in the secondary electron image, these areas correspond to areas of increased density.

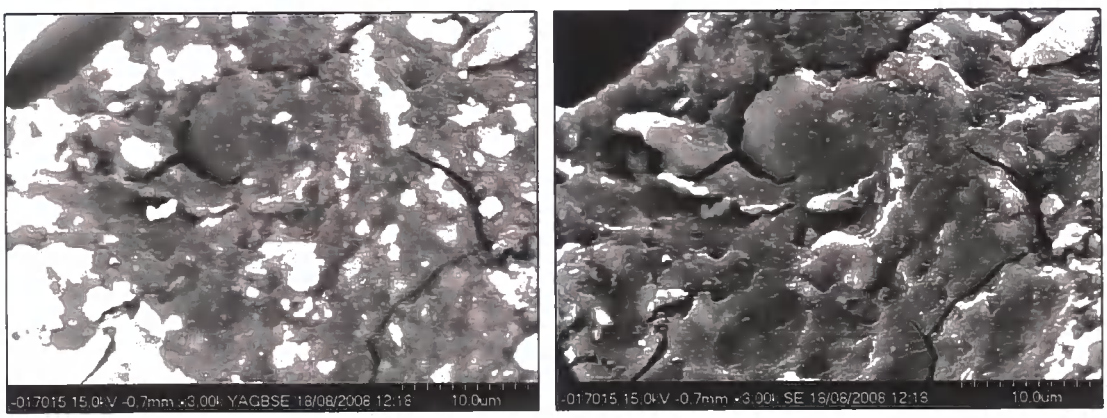

a) b)

Figure 4.23: SEM images of dry Ni_2TCNQ. Electron beam accelerated to 15kV. The length scale is 10μm. Image a) backscattered electron image b) secondary electron image of the same area.

Transmission electron microscopy images reveal small, roughly circular particles of approximately (30-60)±5 nm in size as can be seen in Figure 4.24a. The particles contain small black grains, which may be smaller particulates of approximately 3-5nm in length. It is likely that these black particles are nickel nanoparticles that have grouped together due to the mutual attraction of the magnetic dipoles. Another particulate region which may relate to the matrix of the sample is shown in Figure 4.24b, this region appears to be composed of a polycrystalline material. This area may contain the organic TCNQ or alternatively a mixture of both the organic and the solvent material.

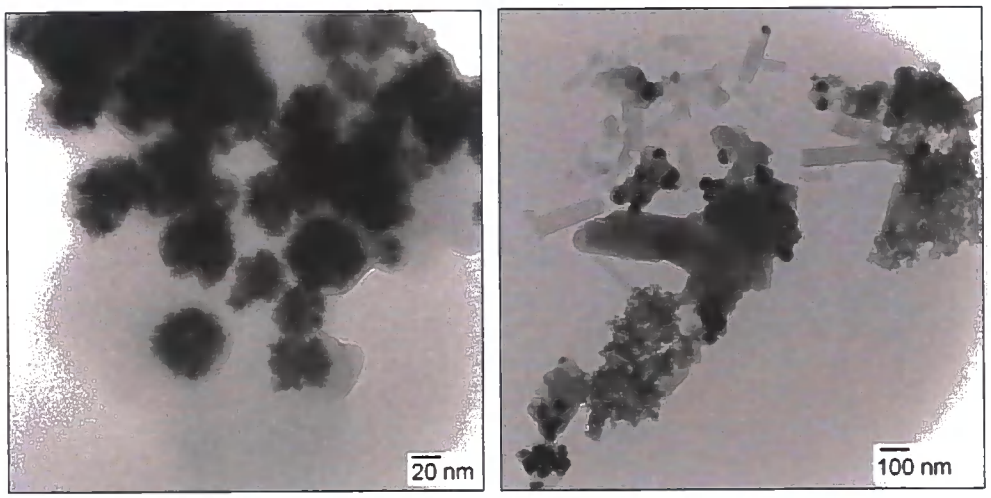

a) b)

Figure 4.24: TEM images of Ni_2TCNQ

It appears in one of the TEM images that chaining of the nickel particles is occurring. Chaining occurs when particles are attracted to one another due to the dipole-dipole interaction. The particles form a chain in order to minimise energy, therefore the overall magnetization of the particle is zero as the various directions of the magnetic moments are cancelled out by others in opposing directions. This effect can be seen in Figure 4.25.

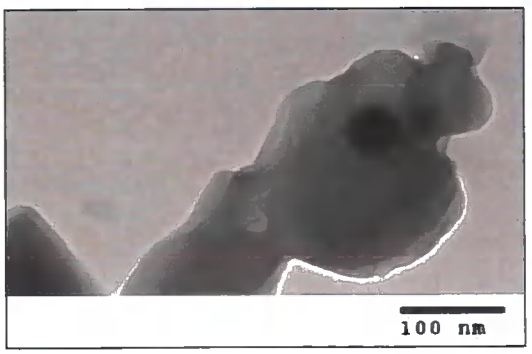

Figure 4.25 TEM image of the dry Ni_2TCNQ sample displaying chaining.

Ni_2TCNQF_4

The calculated values for the elemental analysis are based on those calculated by Jain *et al*[1] with the TCNQ molecule replaced with $TCNQF_4$. An additional test was completed on Ni_2TCNQF_4 to determine the percentage of chlorine in the sample from the solvent (Table 4.8). When compared to the calculated value there was much less percentage chlorine in the sample than expected, thus confirming the presence of little solvent in the material, most having been driven out during synthesis. It was previously thought the low values for carbon, nitrogen etc could be explained by increased solvent in the system, however this is not the case in this material. One possibility is additional oxygen in the sample. The surface of the $Ni(cod)_2$ was oxidised during synthesis and this may explain any additional oxygen in the sample. The percentage carbon in the sample that was not due to Ni_2TCNQF_4 or solvent material was found to be 4.64%. As with the other nickel materials the extra carbon in the sample is likely due to the starting materials.

Element	Calculated %	Found %
C	30.77	29.74
H	1.21	1.31
N	11.84	9.75
Cl	1.87	0.69
Total %	45.69	41.49

Table 4.8: Elemental analysis for the Ni_2TCNQF_4 sample.

The ICP-MS data for Ni_2TCNQF_4 revealed a decrease in the expected percentage value for nickel. This may again be due to an increase in oxygen in the sample. Using nitrogen to calculate the percentage $TCNQF_4$ and the percentage nickel values found using ICP-MS, the ratio of Ni:$TCNQF_4$ was found to be 2.2:1. Even though there is a lower mass percentage of nickel than expected, the ratio of Ni:$TCNQF_4$ is larger than expected, though still comparable to that observed with the wet and dry Ni_2TCNQ samples. This may be due to a loss of $TCNQF_4$ during synthesis.

Element	Calculated %	Found %
Ni	24.81	22.31

Table 4.9: ICP-MS data for the Ni_2TCNQF_4 sample.

TGA of Ni_2TCNQF_4 revealed a percentage weight change corresponding to water loss between 300 and 500K. The sample also shows a second stage of decomposition at 620K (Figure 4.26a), although this appears similar to the Ni_2TCNQ samples the onset of this decay is much less pronounced. At the highest temperature measured (1272K) the sample is still decaying at a constant rate. The final percentage change is also lower than that of both Ni_2TCNQ samples. The TGA of the Ni_2TCNQF_4 is inherently different to the other samples.

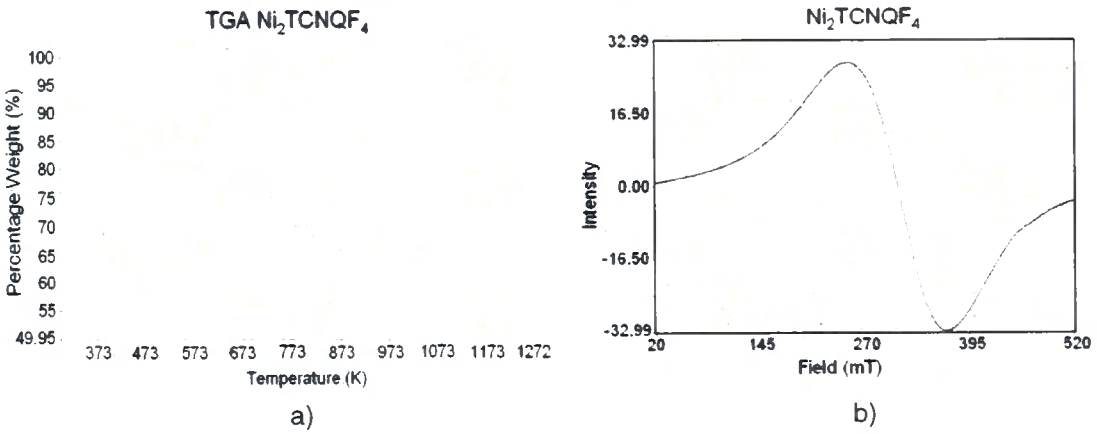

Figure 4.26: a) TGA of Ni_2TCNQF_4 b) ESR spectrum of Ni_2TCNQF_4

The room temperature ESR spectrum revealed a large absorption across a wide magnetic field range. The field was scanned between 0.02 and 0.52T as can be seen in Figure 4.26b. The signal is asymmetric with a linewidth of 0.12T. The broadness of the signal may indicate interactions between the types of spins centres.

Magnetic Measurements

The $M(T)$ plots with FC and ZFC curves for Ni_2TCNQF_4 can be seen in Figure 4.27a. The ZFC curve displays a blocking temperature of approximately (300±5) K. This blocking temperature is much higher than seen for previous samples and may be a result of either larger particles in the sample or an increase in the magnetocrystalline anisotropy. Using extrapolated values the Curie temperature is estimated to be (423±5) K.

To accurately determine the Curie temperature the sample was heated in stages and field sweeps recorded after each consecutive temperature. The sample was heated

to a maximum temperature of 630K, the data for which can be seen in Figure 4.27b. The magnetization was recorded as the sample was cooled from 630K to 300K at a rate of 10K/min. Although this experiment is effectively a field cooled experiment there should be no difference to a zero field cooled experiment as at high temperatures the curves overlay as shown in Figure 4.27a.

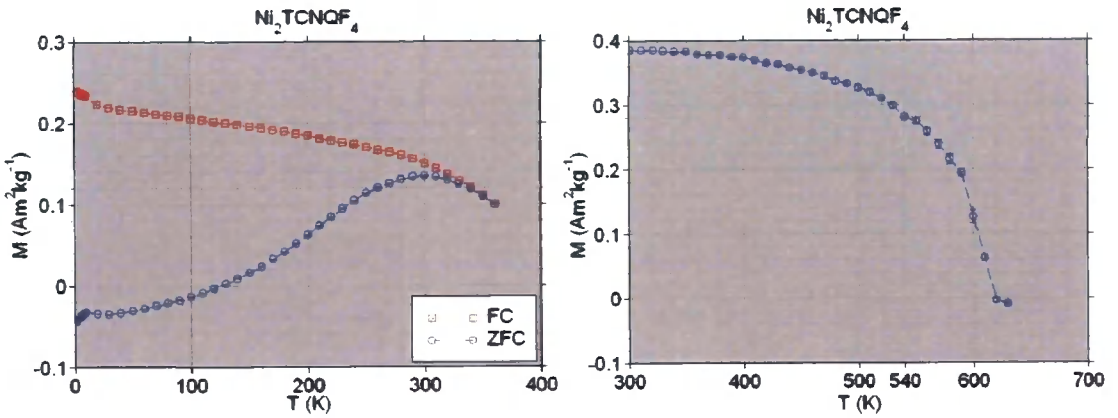

a) b)

Figure 4.27: $M(T)$ curves for Ni_2TCNQF_4.with an applied field of $\mu_0 H$=2.5mT. a) Temperatures up to 360K and a heating rate of 10K/min. b) Temperatures up to 630K with a heating rate of 1K/min.

The Curie temperature is found to be (620±5) K, which is much higher than the extrapolated value indicates. There is also a dip in the data at approximately 540K, which may be another Curie temperature superimposed on the data. If so, this could potentially indicate that there is another component in the material that is magnetically ordered and has a transition temperature well above room temperature. Both features in Figure 4.27b are analogous to those observed for wet Ni_2TCNQ as shown in Figure 4.16.

The $M(H)$ loop recorded at 630K shows paramagnetic behaviour, as expected for a material heated past its Curie temperature.

$M(H)$ loops reveal a strong paramagnetic component at high field values. It appears from first impressions that this system is exhibiting two magnetic phases as was observed with the Ni_2TCNQ samples.

The magnetization was investigated at low fields to probe the nanoparticulate contribution to the magnetism and can be seen in Figure 4.28. The sample exhibits

large coercive fields (51mT at 2K) and a remanent component at low temperatures. The loop shown in Figure 4.28a has not yet reached saturation. Further experiments to determine the saturation magnetization revealed that the loop did not fully close until the applied field reached 1T. The sample therefore contains some very magnetically hard particles with large coercivities. The loops also show a slight shift ((0.3-3.7) mT) towards more negative field values. This could be due to exchange bias effects.

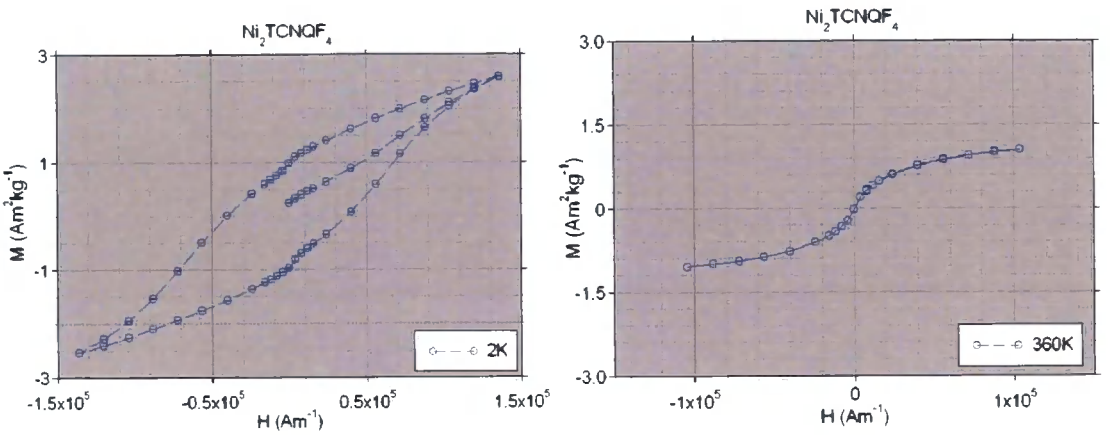

a) b)

Figure 4.28 $M(H)$ loops for Ni_2TCNQF_4 a) 2K b) 360K.

At high temperatures (above the blocking temperature- Figure 4.28b) the sample exhibits superparamagnetism. Accordingly the system displays no remanence or coercivity.

$M(H)$ loops were also recorded in high applied fields ($\mu_0 H$=5T) and measured at a variety of temperatures to probe the paramagnetic component (Figure 4.29a). The $M(H)$ loops are typical of soft magnetic materials.

The paramagnetic data was compared to a Brillouin function (Figure 4.29b) with J=1, θ=-(0.4±0.3) K, N=(8.7±0.2)x10^{23} kg^{-1} and $M_{s(Nano)}$=(2.9±0.1) Am^2kg^{-1} (The value for $M_{s(Nano)}$ was taken from low field data where the nanoparticulate contribution dominates the magnetism). From elemental analysis the number of nickel atoms per kilogram is estimated to be 2.29x$10^{24}kg^{-1}$. The value for θ is small, suggesting that the spins are very weakly interacting. The negative θ value implies that the interaction between the spins is antiferromagnetic. The fit is poor at lower fields due to the nanoparticulate contribution.

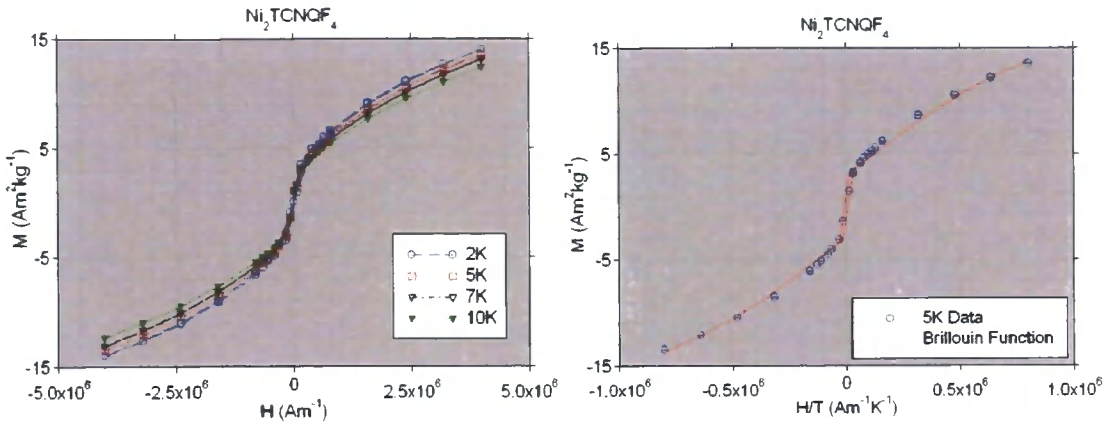

Figure 4.29: a) $M(H)$ loops for Ni_2TCNQF_4 at low temperatures. b) $TCNQF_4$ 5K high field data with Brillouin function, J=1.

As with the previous nickel samples the $M/M_{s(Para)}$ against $H/(T\text{-}\theta)$ fits required $M_{s(Para)}$ to be altered as a function of temperature for the curves to superimpose, as shown in Figure 4.30.

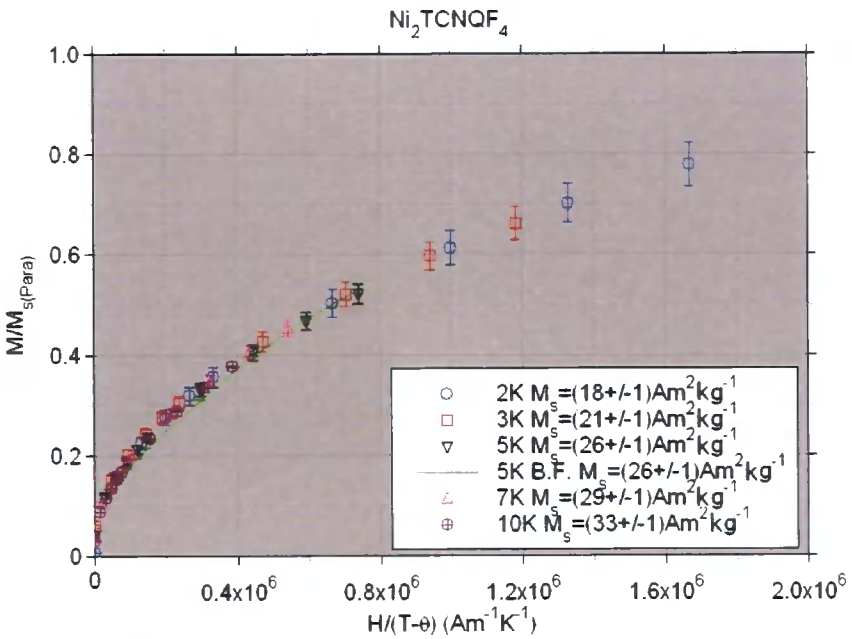

Figure 4.30: $M/M_{s(Para)}$ versus $H/(T\text{-}\theta)$ for Ni_2TCNQF_4 at various temperatures.

As the shape of the curve is not changing, this implies that the J value is equal to one. The increase in $M_{s(Para)}$ as a function of temperature is indicative of a spin transition from a low spin state to a high spin state.

X-ray Diffraction

The X-ray diffraction data for Ni_2TCNQF_4 can be seen in Figure 4.31. The data in Figure 4.31b has been corrected for the background contribution from the glass holder. Glass is amorphous therefore a large signal is superimposed upon the data before analysis (Figure 4.31a). The background was subtracted automatically by comparing the slope of the peaks relative to each other. Although this allows attempts to fit the data, the removal of the background signal may have removed any amorphous component that may have been produced by the sample itself as was reported by Jain *et al*[1].

The peak at approximately 44° relates to nickel in the sample. Using the width of the peak and the Scherrer equation[41] (Appendix A4) it was possible to estimate the mean separation of the planes for the peak associated with nickel. This analysis gave an average particle size of (2.9±0.4) nm.

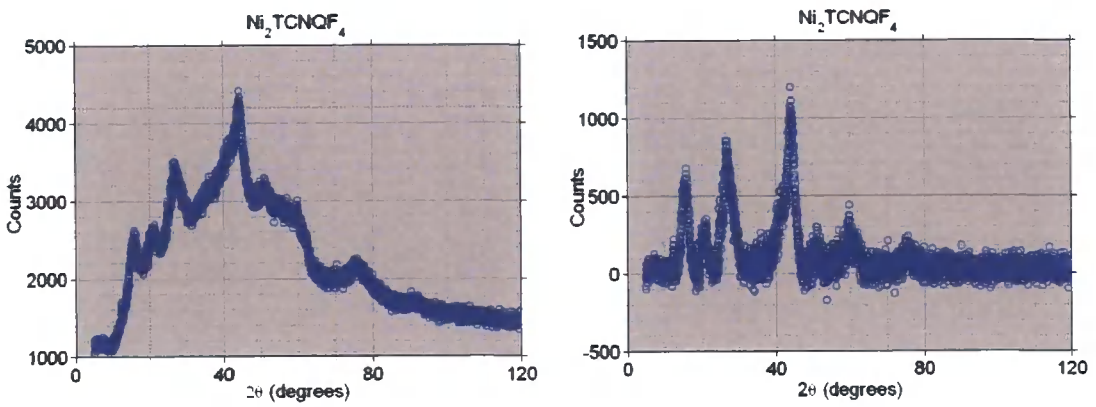

Figure 4.31: a) XRD data for the Ni_2TCNQF_4 sample, uncorrected for background. b) Data corrected for background signal.

An estimate for particle size can also be calculated using Equation 9. This requires the anisotropy for nickel ($5.1x10^3 Jm^{-3}$)[10] and the experimentally found blocking temperature (300±5) K. This reveals an estimated particle size of (27.2±0.2) nm.

Microscopy Images

Scanning electron microscopy and transmission electron microscopy was carried on the Ni_2TCNQF_4 sample. The particle sizes ranged between 500μm to larger than

1000μm. (The minimum resolution of the microscope was x100 and this was too high to image the sizes of the larger particles). The surface of the particles displays cracks and an uneven texture. The particles also reveal what appears to be a structured layering as can be seen in Figure 4.32b.

The backscattered electron image displays evidence of increased areas of nuclei, most likely corresponding to nickel particles (Appendix A5). The backscattered electron image was compared to the secondary electron image to confirm that the brighter areas in the image did not relate to the topology of the structure.

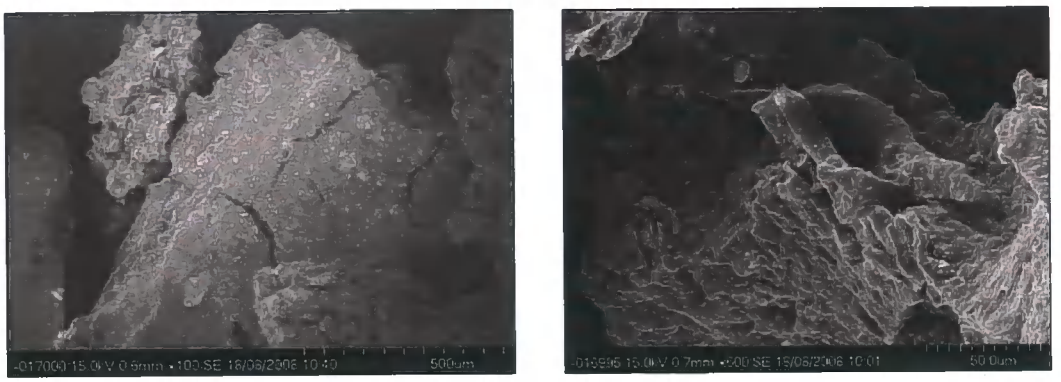

a) b)

Figure 4.32: SEM images of Ni_2TCNQF_4. Images a) and b) were taken from different areas of the sample.

The TEM images display large dense areas of sample (Figure 4.33). From the images there appears to be two different types of particle present. The darker more dense particles are likely to be nickel. There are also small particulates within the darker regions, which could be small grains, approximately 1-3 nm in length. This corresponds to the XRD data which gives the nanoparticulate grain sizes of (2.9±0.4) nm. The other areas in the image may correspond to the samples matrix, this material appears poly-crystalline with particle sizes of in the order of 10-20nm.

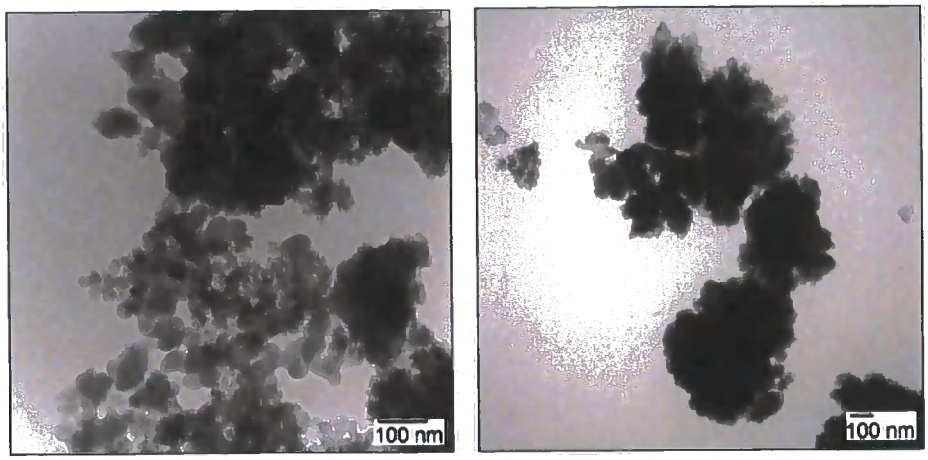

Figure 4.33: TEM images of Ni_2TCNQF_4.

5. Discussion

Organic Acceptors

Most of the organic molecules investigated display expected properties of systems with free radicals present. With the exception of MSzJ25 and $TCNQF_4$ the samples were all diamagnetic at room temperature with paramagnetic behaviour at low temperatures described by small negative Weiss constants, as expected[12]. NaTCNQ was arguably the most interesting organic system investigated, with the material undergoing a spin transition between 2 and 300K. At low temperatures, the paramagnetism of the material could be modelled by the Brillouin function with J=1/2, this analysis revealed a Curie Weiss constant of (-0.85±0.14) K. The room temperature ESR measurements also revealed hyperfine interactions in the sample suggesting that the electrons are interacting with their environment.

$TCNQF_4$ was chosen as a good candidate for the synthesis of a new magnetic material as it is highly electronegative and a smaller molecule than many of the other organics. A smaller molecule allows the spin sites to be spatially closer together thus encouraging interactions and providing a higher spin density. $TCNQF_4$ is also paramagnetic across the entire temperature range examined (2-300K).

Ni_2TCNQ

From the infrared, ESR and TGA data it appears that the wet and dry Ni_2TCNQ samples are very similar. The most notable differences between the samples are the elemental analysis results and a small variation in magnetic properties. Elemental analysis suggests that the dry sample contains less solvent, which most likely occurs due to the processing of the material after synthesis. The elemental analysis also suggests there is an increase in the ratio of Ni:TCNQ in the dry sample over that of the wet material. This may again be due to the difference in how the samples were obtained. When the materials are in solution, small black particulates are formed after exposure to air. It is possible that the larger particles are simply formed due to the mutual attraction of the smaller magnetic particles. When the sample is filtered it is these larger particles that form the dry sample. The particulates that precipitate out of the solution after 24 hours are then collected to form the wet sample. As the wet sample was not dried in a vacuum it is likely to contain slightly increased solvent and oxygen species.

Both the wet and dry Ni_2TCNQ samples exhibit two magnetic phases. The samples are superparamagnetic above the blocking temperature and at low temperatures exhibit single domain behaviour. There are a number of small, but significant, differences in the magnetic properties of wet and dry Ni_2TCNQ. Dry Ni_2TCNQ has both a larger blocking temperature and higher coercive field values than wet Ni_2TCNQ. These differences can be explained due to an increase in the average size of the particles. It therefore appears that the wet and dry samples are likely the same, but with a different average particle size.

The Curie temperature for wet Ni_2TCNQ was found to be (625±5) K, this is extremely close for the value reported for nickel (631K)[10]. It is likely that the particles responsible for the low field data are nickel nanoparticles. This analysis is further supported by the backscattered electron images recorded with SEM, as the images show areas of increased density that most probably correspond to nickel. The TEM images reveal small particulates of (3-5) nm which are almost certainly nickel. $Ni(cod)_2$ has been reported to form nickel nanoparticles[42], of approximately 5nm, in an amorphous carbon matrix, the TEM images of which can be seen in Appendix A6. Although it should be noted that the nanoparticles created by Koltypin *et al*[42] were formed by sonochemical techniques and heating the $Ni(cod)_2$ above the crystallisation temperature of 873K. If the nanoparticles in the Ni_2TCNQ samples were contained in a carbon matrix it would support the conclusion that the additional carbon is from the $Ni(cod)_2$ starting material.

Ni_2TCNQF_4

As with Ni_2TCNQ the magnetic data for Ni_2TCNQF_4 displays two distinct magnetic phases. The sample is superparamagnetic above the blocking temperature and exhibits single domain behaviour at low temperatures. The presence of nickel nanoparticles is supported not only by the magnetic data but microscopy measurements and XRD data. The Curie temperature was found to be (620±5) K which, as with the other samples, indicates the presence of nickel. The XRD data supports the evidence for the presence of nickel and by using the Scherrer equation the estimated size of the nanoparticles was found to be (2.9±0.4) nm. This is similar to a value estimated from XRD data of 3.2nm for nickel nanoparticles synthesized from $Ni(Cod)_2$[42].

Electron microscopy measurements, and the increase in blocking temperature for Ni_2TCNQF_4, indicate that the Ni_2TCNQF_4 sample contains larger particles than the Ni_2TCNQ samples. This conclusion is also supported by the higher coercivities exhibited by Ni_2TCNQF_4. Although this is likely due to the increase in particle size, alternatively there may be an increase in the magnetocrystalline anisotropy in the material.

At low temperatures, all the molecular magnets investigated appear to exhibit a spin transition in the paramagnetic phase, from a low spin state to a high spin state. The Brillouin function fitting for Ni_2TCNQ reveals that the spins are weakly interacting ferromagnetically. On the other hand, Ni_2TCNQF_4, shows even weaker interactions between the spins with theta having a smaller magnitude and negative sign indicating that the spins are coupling antiferromagnetically.

The high temperature magnetic data determined the Curie temperatures for wet Ni_2TCNQ and Ni_2TCNQF_4 as (625±5) K and (620±5) K respectively. Both samples appear to exhibit small anomalies in the $M(T)$ curves at 530 and 540K. This may indicate additional components in the samples that have transition temperatures above room temperature. This component may arise from nickel that has successfully been coordinated with the organic acceptor molecules. The main observation to note is that the temperature at which this anomaly occurs is different for the Ni_2TCNF_4 and Ni_2TCNQ samples.

6. Conclusion

The molecular magnet Ni_2TCNQ has been synthesized and characterised. Originally two variations of Ni_2TCNQ were produced, a wet and dry sample. After careful analysis it was assumed that these samples are identical except for the average particle size. The characterisation of this material contradicted current literature[1] which claims that the material is a spin glass and that the magnetism arises from coordination between the nickel and TCNQ moiety.

This research suggests that there at least two magnetic phases present in Ni_2TCNQ. The material is superparamagnetic above the blocking temperature and exhibits single domain behaviour at low temperatures. These particles are embedded in a paramagnetic matrix which dominates the magnetism at high magnetic fields. Magnetic measurements and microscopy indicate that the samples contain nickel nanoparticles. However to fully characterise the samples XRD data is required to confirm the presence of nickel.

A new molecular magnet was designed from an investigation into various organic acceptor molecules. The resultant magnet, Ni_2TCNQF_4 was synthesized and characterised using various techniques. As with the previous molecular magnet this sample exhibits superparamagnetism and single domain behaviour at low temperatures. In high magnetic fields the sample is paramagnetic and it is assumed that the paramagnetism arises from the samples matrix. The XRD data revealed that the material contains nickel nanoparticles. This was further confirmed by the experimentally determined Curie temperature and microscopy measurements.

It is possible that a contribution to the magnetism arises from nickel that has been coordinated to the organic acceptor molecules, this is shown by anomalies in the high temperature magnetic data. These results may indicate an additional Curie temperature that corresponds to a magnetically ordered phase in the material that is not related to nickel nanoparticles. The postulated Curie temperatures are 530 and 540K for Ni_2TCNQ and Ni_2TCNQF_4 respectively. It is possible that the difference in temperatures is caused by the change in organic moiety in each system. If this component in the system could be isolated it may be possible to tune the magnetic properties, i.e. the Curie temperature, through choice of organic acceptor molecule.

7. References

1. Jain, R., et al.'High-temperature metal-organic magnets'. *Nature*, 2007, 445(7125), pp. 291-294.
2. Long G., Willett R.D. 'Electrochemical synthesis, characterization and magnetic studies of Ni/TCNQ salts', *Inorganica Chimica Acta*, 2001, 313(1-2), pp.1-14.
3. Heisenberg, W. 'Zur Theorie des Ferromagnetismus', *Z. Phys*, 1928, 49 pp. 619-636.
4. Miller J.S., Epstein A.J. 'Organometallic magnets', *Coordination Chemistry Review*, 2000, 206, pp. 651-660.
5. Miller, J.S., et al. 'Ferromagnetic behavior of $[Fe(C_5Me_5)_2]^{+}[TCNE]^{-}$Structural and Magnetic Characterization of Decamethylferrocenium Tetracyanoethenide, $[Fe(C_5Me_5)_2]^{+}[TCNE]^{-}$•MeCN and Decamethylferrocenium Pentacyanopropenide, $[Fe(C_5Me_5)_2]^{+}[C_3(CN)_5]^{-}$ ', *Journal of American Chemical Society*, 1987, 109(3), pp. 769-781.
6. Miller, J.S., Epstein, A.J. 'Tetracyanoethylene-based organic magnets', *Chemical Communications*, 1998, 13, pp. 1319-1325.
7. Crayston J.A., Devine J.N., Walton J.C. 'Conceptual and Synthetic Strategies for the Preparation of Organic Magnets', *Tetrahedron*, 2000, 56(40),pp..7829-7857.
8. Miller J.S. 'Organometallic and Organic-Based magnets:New Chemistry and New Materials for the New Millenium', *Inorganic Chemistry*, 2000 39(20), pp.4392-4408.
9. Crangle J. *Solid State Magnetism*. Great Britain:Edward Arnold, 1991
10. Jiles D. *Introduction to magnetism and magnetic materials*. Chapman & Hall. 1st ed, 1998.
11. Ruderman, M.A., Kittel, C, et at. ' Indirect Exchange Coupling of Nuclear Magnetic Moments by Conduction Electrons', *Physical Review*, 1954, 96(1), pp. 99-102.
12. Kittel, C. *Introduction to solid state physics*. USA:John Wiley and Sons, 7th ed, 2005.
13. Iglesias, O., Batlle, X., Labarta, A. 'Modelling exchange bias in core/shell nanoparticles', *Journal of Physics-Condensed Matter*, 2007, 19(40).
14. Iglesias, O., Batlle, X., Labarta, A. 'Exchange bias and asymmetric hysteresis loops from a microscopic model of core/shell nanoparticles', *Journal of Magnetism and Magnetic Materials*, 2007, 316(2), pp. 140-142.
15. Kahn, O. *Molecular Magnetism*. USA: VCH Publishers, 1993.
16. Stoner, E.C., Wohlfarth, E.P. 'A Mechanism of Magnetic Hysteresis in Heterogeneous Alloys', *Philosophical Transactions of the Royal Society of London Series A- Mathematical and Physical Sciences*, 1948, 240(826), pp. 599-642.

17. Kronmüller, H., Parkin, S. *Handbook of Magnetism and Advanced Magnetic Materials: Volume 4: Novel Materials.* Barcelona:John Wiley and Sons, 2007.
18. Leslie-Pelecky D.L., Rieke R. 'Magnetic properties of Nanostructured Materials', *Chemistry of Materials*, 1996, 8(8), pp.1770-1783.
19. Mydosh, J.A. *Spin Glasses: An Experimental Introduction.* CRC, 1993.
20. McConnell, H.M. ' Ferromagnetism in Solid Fee Radicals', *Journal of Chemical Physics*, 1963, 39(7), pp. 1910-1911.
21. Miller, J.S., et al. 'Synthesis and Characterization of the Metamagnetic 1:1 1-D Phase of the Decamethylferrocenium 7,7,8,8-tetracyano-*p*-quinodimethanide: $Fe[C_5(CH_3)_5]_2^{+\bullet}(TCNQ)^{-\bullet}$', *Journal of the American Chemical Society*, 1979, 101(23), pp. 7111-7113.
22. Zhang, J., et al. '$[M^{II}(tcne)_2]$ $x CH_2Cl_2$ (M=Mn, Fe, Co, Ni) Molecule-Based Magnets with Tc Values Above 100 K and Coercive Fields up to 6500 Oe', *Angewandte Chemie-International Edition*, 1998, 37(5), pp. 657-660.
23. Vickers, E.B., Senesi, A., Miller, J.S. '$Ni[TCNE]_2 \cdot {}_zCH_2Cl_2$ (T_c=13 K) and $V_xNi_{1-x}[TCNE]_y \cdot {}_zCH_2Cl_2$ solid solution room temperature magnets', *Inorganica Chimica Acta*, 2004, 357(13), pp. 3889-3894.
24. Clerac R. et al. 'Glassy Magnets composed of Metals Coordinated to 7,7,8,8-tetracyanoquinodimethane: M(TCNQ)2 (M=Mn, Fe, Co, Ni)', *Chemistry of Materials*, 2003, 15(9), pp.1840-1850.
25. Pokhodnya, K.I. et al. 'Effect of solvent on the magnetic properties of the high-temperature V.TCNE.*x* molecule-based magnet', *Physical Review B*, 2001, 63(17)
26. Miller J.S., Pokhodnya K.I. 'Formation of Ni(C4(CN)8) from the reaction of Ni(COD)2 (COD=1,5-cyclooctadiene) with TCNE in THF', *Journal of Materials Chemistry*, 2007, 17(34), pp.3585-3587
27. Webster, O. W.. Mahler, W, Benson, R.E. 'Chemistry of Tetracyanoethylene Anion Radical' *Journal of the American Chemical Society,* 1962, 84 (19), pp. 3678-3684.
28. Makarova, T.L. 'Magnetic carbon (Retraction vol 413, pg 716, 2001)', *Nature*, 2006, 440(7084) pp. 716–718.
29. Van Noorden, R. 'Magnetic dreams disputed', *Chemistry World*, 4(10), pp.23-23.
30. Acker D.S., Hertler W.R. 'Substituted Quinodimethans. 1. Preparation and Chemistry of 7,7,8,8-Tetracyanoquinodimethan', *American Chemical Society*, 1962, 84(17), pp.3370-3373.
31. Rafael G., Carlos S., Segura J.L. 'The first two decades of a versatile electron acceptor building block: 11,11,12,12-tetracyano-9,10-anthraquinodimethane (TCAQ)', *Chemical Society Reviews*, 2007, 36(8), pp.1305-1302.
32. Wertz J.E., Bolton J.R. *Electron Spin Resonance Elementary Theory and Practical Applications.* Chapman and Hall, 1972.

33. Quantum Design, 2000. Our products: magnetic property measurement systems, [Online]. Available at: http://www.qdusa.com/products/mpms.html [accessed 10.04.2008].

34. National Institute of Environmental Health Science, 2007. Public electron paramagnetic resonance software tools. [Online]. Available at: http://www.niehs.nih.gov/research/resources/software/tools/index.cfm [accessed 01.11.2007]

35. Blackmore, J.S. *Solid State Physics* . Cambridge University Press, 1985.

36. Konno M.,Saito Y. et al. 'Crystal-Structure of Sodium 7,7,8,8-Tetracyanoquinodimethane', *Acta Crystallographica Section B-Structural Science*, 1974, B30, pp.1294-1299

37. Vickers, V.B., Giles, I.D., Miller, J.S. 'M[TCNQ]$_y$-Based Magnets (M= Mn, Fe, Co, Ni; TCNQ= 7,7,8,8-tetracyano-*p*-quinodimethane)', *Chemistry of Materials*, 2005, 17(7), pp.1667-1672.

38. Decrutins, S. et al. 'Light-Induced Excited Spin Trapping in a Transition-Metal Complex-The HEXA-1-Propyletrazole-Iron (II) Tetrafluoroborate Spin-Cossover System', *Chemical Physics Letters*, 1984, 105(1), pp. 1-4.

39. Gütlich, P., Ksenofontov, V., Gaspar, A.B. 'Pressure effect studies on spin crossover systems', *Coordination Chemistry Reviews*, 2005, 249(17-18) pp. 1811–1829.

40. Kaye, G.W.C., Laby T.H., *Tables of Physical and Chemical Constants.* USA:Longman Group Limited, 1986.

41. Klung, H., Alexander, L. X-ray *Diffraction Procedures.* New York: Wiley, 1962 pp. 491.

42. Koltypin, Y. 'Encapsulation of Nickel Nanoparticles in Carbon Obtained by the Sonochemical Decomposition of $Ni(C_8H_{12})_2$', *Chemistry of Materials*, 1999, 11(5), pp.1331-1335.

8. Appendix

A1

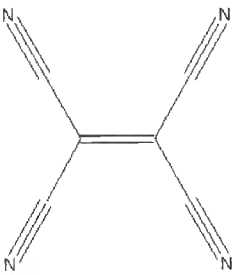

TCNE molecule.

A2

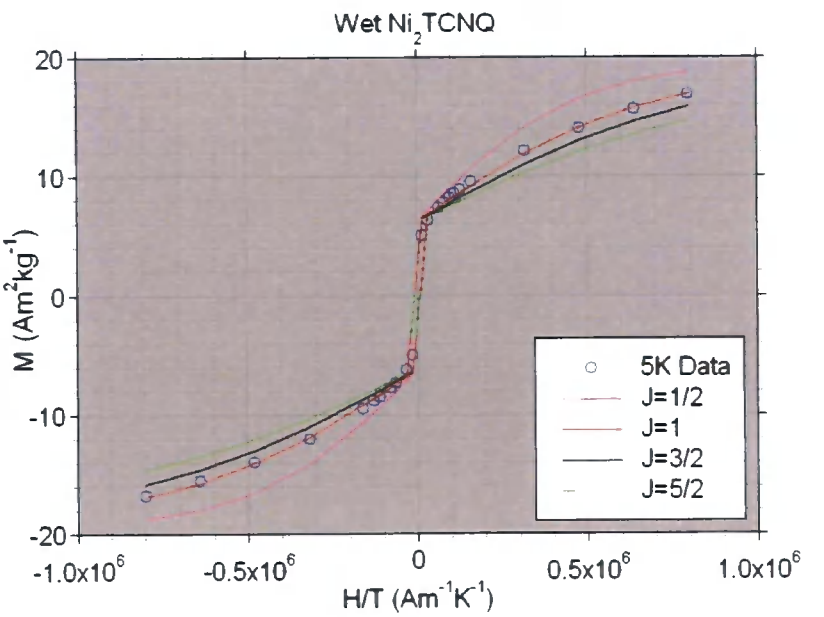

Alternate J values for Brillouin function with θ=1.1K, $M_{s(Nano)}$=6.2 Am^2kg^{-1}

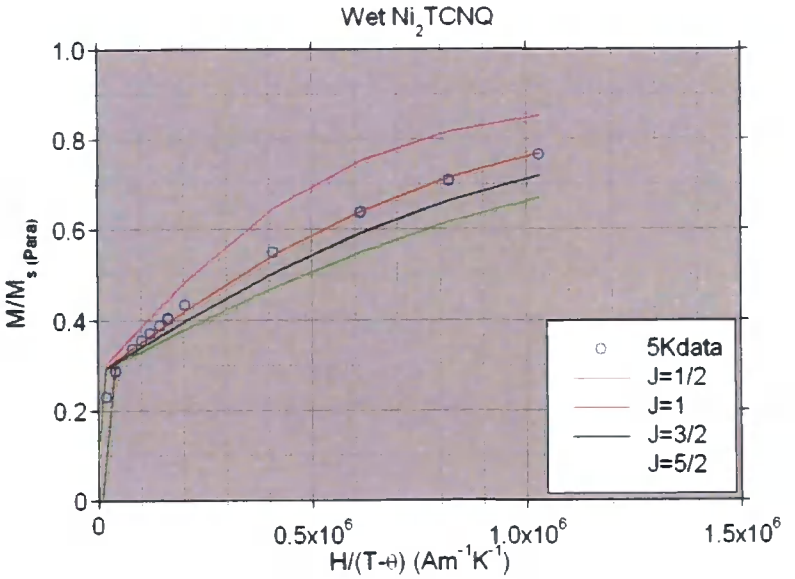

Influence of alternate J values for Brillouin function when M is divided by the paramagnetic saturation magnetization with θ=1.1K, $M_{s(Nano)}$=6.2 Am^2kg^{-1}, $M_{s(Para)}$=22 Am^2kg^{-1}.

A3

SEM images of Ni_2TCNQ: Layered structure.

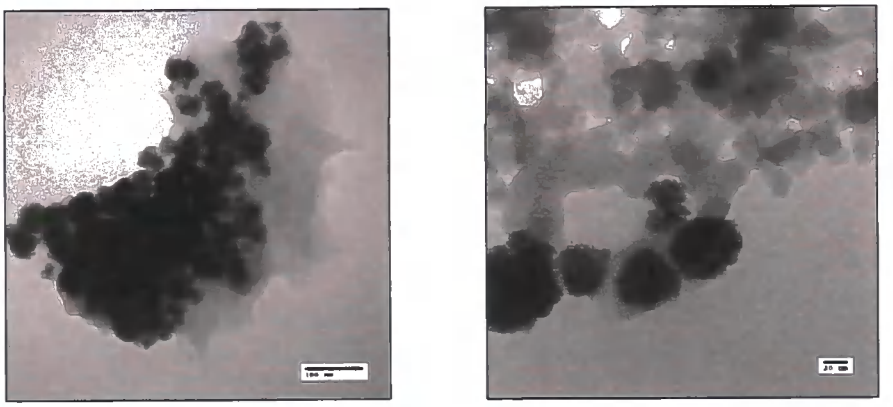

TEM images of dry Ni_2TCNQ

A4

Scherrer Equation

This analysis assumes that the broadness of the peaks arises due to small crystallite size alone and calculates the average size.

$$L = \frac{K\lambda}{\beta \cos\theta}$$

Where L is the mean dimension of the particles, λ is the X-ray wavelength, θ is the position of the peak, K is a constant equal to approximately one and β is the full width half maxima in 2θ units.

A5

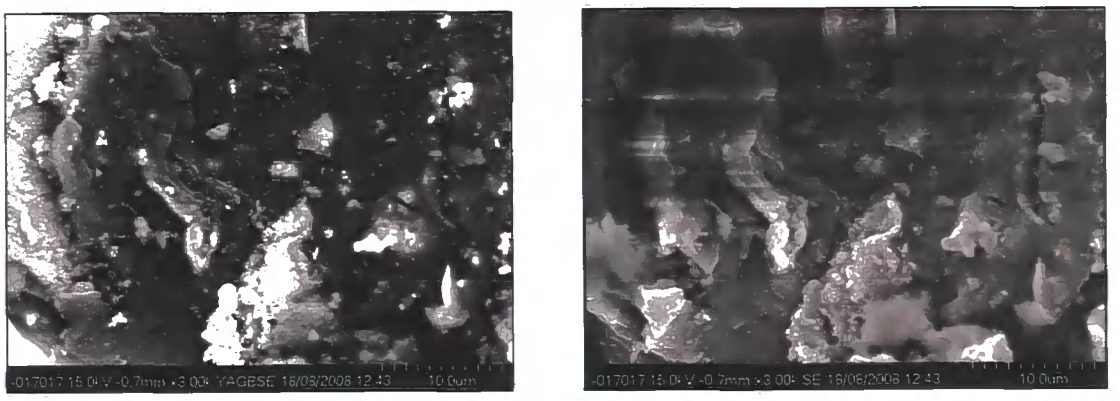

a) b)

a) Backscattered image of Ni_2TCNQF_4 b) Secondary electron image of same area.

A6

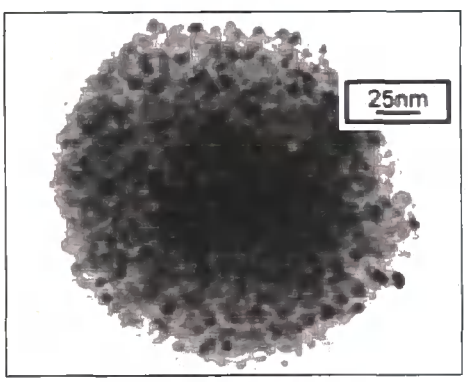

Encapsulation of nickel nanoparticles in carbon obtained by sonochemical decomposition of $Ni(cod)_2$ (Kolltypin et al [42])


UNIV
DUKE
ELM